Remote Sensing of Environment 347 (2026) 115684

Contents lists available at ScienceDirect

Remote Sensing of Environment

journal homepage: www.elsevier.com/locate/rse

Retrieval of nighttime oceanic liquid cloud optical and microphysical parameters from VIIRS observations: a physics-informed machine learning approach

Ying-Chieh Chen [a], Meng Zhou [a,b,*], Jun Wang [a,c,*], Xi Chen [a,c], Jing Zeng [a,c], Yongxiang Hu [d]

[a] Department of Chemical and Biochemical Engineering, The University of Iowa, Iowa City, IA, USA
[b] Goddard Earth Sciences Technology and Research, University of Maryland, Baltimore County, Baltimore, MD, USA
[c] Center for Global and Regional Environmental Research and Iowa Technology Institute, The University of Iowa, Iowa City, IA, USA
[d] Science Directorate, NASA Langley Research Center, Hampton, VA, USA

ARTICLE INFO

Edited by: Menghua Wang

Keywords:
Nighttime cloud retrieval
VIIRS DNB
Machine learning retrieval
Cloud optical thickness (COT)
Cloud effective radius (CER)
Cloud microphysics
Physics-informed modeling

ABSTRACT

Accurate retrieval of nighttime water cloud optical and microphysical properties, including cloud optical thickness (COT) and cloud effective radius (CER), remains a long-standing challenge. This study develops a physics-informed machine-learning framework, UI-Cloud (Unified Illumination Cloud Microphysics Retrieval Framework), to retrieve nighttime oceanic liquid-cloud COT and CER from observations of the Visible Infrared Imaging Radiometer Suite (VIIRS). The framework unifies solar and lunar illumination regimes by training on daytime data and applying physically constrained corrections to nighttime radiance inputs. The VIIRS Day/Night Band (DNB) top-of-atmosphere reflectance serves as a bridging variable linking daytime and nighttime conditions. Lookup tables generated using the UNified Linearized Vector Radiative Transfer Model (UNL-VRTM) quantify day–night brightness temperature (BT) offsets and enable dynamic correction of residual solar contributions in the 4.065 μm thermal emissive band (M13).

The daytime model demonstrates strong agreement with VIIRS standard retrievals ($R = 0.98$). Direct application to nighttime data results in CER overestimation, whereas incorporation of the UNL-VRTM-based M13 BT correction yields nighttime global mean values (COT = 16.0; CER = 16.8 μm) that are consistent with daytime references (14.6 and 15.9 μm). Validation against liquid water path (LWP) retrievals from the Advanced Microwave Scanning Radiometer 2 (AMSR2) demonstrates RMSE reduction from 261.9 to 147.9 g m^{-2} and bias decrease from 180% to 62%. Retrieval accuracy is high for Moon Illumination Fraction (MIF) above 70% and remains robust down to approximately 50%, enabling the UI-Cloud framework to extend diurnal cloud optical and microphysical observations beyond daytime-only conditions into lunar-illuminated nights.

1. Introduction

Clouds significantly influence Earth's energy budget by modulating the amount of shortwave and longwave radiation that reaches the surface or escapes back into space (Ramanathan, 1987; Ramanathan et al., 1989). Cloud optical thickness (COT) and cloud effective radius (CER) are important optical and microphysical properties for understanding aerosol-cloud-precipitation interactions and improving the accuracy of climate modeling and weather forecasts (Fan et al., 2016; Tao et al., 2012). CER, in particular, reflects how aerosols influence cloud droplet size, as described by the "Twomey" effect, where increased aerosols result in smaller, more numerous droplets for a constant liquid water path, enhancing cloud reflectance (albedo) (Twomey, 1977). This reduction in droplet size also extends cloud lifetime and increases cloudiness (Albrecht, 1989) while reducing precipitation efficiency (Rosenfeld, 1999). If ambient conditions favor deep convection, smaller liquid water droplets are more easily uplifted to form ice particles, which in turn may lead to more severe weather (Wang et al., 2009). Retrieving COT and CER at night is essential for capturing cloud properties across the full diurnal cycle, as nighttime aerosol-cloud interactions may differ significantly from daytime due to enhanced longwave cooling, altered turbulent mixing, and a lack of solar heating, all of which influence cloud thickness, liquid water path, and precipitation dynamics (Chen et al., 2011).

* Corresponding authors.
E-mail addresses: meng-zhou-1@uiowa.edu (M. Zhou), jun-wang-1@uiowa.edu (J. Wang).

https://doi.org/10.1016/j.rse.2026.115684
Received 9 March 2026; Received in revised form 3 September 2026; Accepted 14 September 2026
Available online 24 September 2026

Despite their importance, nighttime cloud optical and microphysical retrievals from space remain one of the challenges in the field of satellite remote sensing of the atmosphere. Traditional methods for retrieving COT and CER rely on the bi-spectral solar reflectance technique developed by Nakajima and King (1990). In this framework, COT is primarily derived from non-water-absorbing visible and near-infrared (VIS/NIR) wavelengths (e.g., 0.67, 0.87 μm), while CER is inferred from water-absorbing shortwave-infrared (SWIR) wavelengths (e.g., 1.6, 2.1, 3.7 μm), highly sensitive to droplet size. This bi-spectral method has been widely used for passive remote sensing of clouds and serves as the foundation for many modern algorithms for cloud retrievals from the Advanced Very High Resolution Radiometer (AVHRR) (Kawamoto et al., 2001) and the Moderate Resolution Imaging Spectroradiometer (MODIS) (Platnick et al., 2016) to the Visible Infrared Imaging Radiometer Suite (VIIRS) (Platnick et al., 2016) and more, but it has not been applied at night due to the lack of shortwave measurements. This limitation leads to a gap in global nighttime cloud climatology, preventing the study of aerosol–cloud interaction processes at night during the full cloud life cycle. Several recent efforts have attempted to overcome this gap. Walther et al. (2013) followed the daytime bi-spectral retrieval concept by combining lunar reflectance derived from the VIIRS Day-–Night Band (DNB) (0.5–0.9 μm) with thermal emission measured by the 3.75 μm (M12) channel. They showed that compensation between cloud emissivity and transmission, whereby their opposing effects on thermal radiance reduce the sensitivity to effective radius, can create a “blind spot” regime in which thermal radiance becomes weakly sensitive to effective radius. The location of this blind spot depends on COT as well as cloud-top temperature, surface temperature, and their temperature contrast, highlighting the challenges of constraining cloud optical and microphysical properties from nighttime bi-spectral observations alone.

Here, we introduce UI-Cloud (Unified Illumination Cloud Microphysics Retrieval Framework), a neural-network-based framework that unifies daytime and nighttime retrievals using multi-band VIIRS observations to retrieve COT and CER. Recent advances in artificial intelligence (AI) have accelerated the use of machine-learning (ML) models in cloud remote sensing, enabling improved retrievals of both macro- and microphysical properties. Yang et al. (2022) applied eXtreme Gradient Boosting (XGBoost) to Himawari-8/AHI infrared radiances to retrieve cloud mask, cloud-top temperature (CTT), cloud-top height (CTH), and cloud phase, while Wang et al. (2022b) used deep neural networks (DNN) to retrieve CTH and ice-cloud COT, achieving improvements over operational algorithms. Compared with ice clouds, for which thermal infrared retrievals of microphysical properties have been more extensively investigated (e.g., Wang et al. (2016b)), relatively few studies have explored the use of thermal infrared observations for liquid-cloud CER retrievals. In cloud microphysics, Minnis et al. (2016) showed that MODIS 3.7, 6.7, 11.0, and 12.0 μm thermal infrared (TIR) channels can be used to retrieve nighttime opaque ice-cloud COT, extending the retrievable range to COT ≈150, although the deepest clouds remain underestimated due to the blackbody behavior of thick clouds. Zhang et al. (2019) and Hu et al. (2021) used Cloud-Aerosol Lidar with Orthogonal Polarization (CALIOP)–MODIS collocations to train neural network models for CER, cloud droplet number concentration (CDNC), liquid water content (LWC), demonstrating the strengths of lidar-constrained learning but limited by CALIOP's narrow swath and not retrieving COT. Wang et al. (2022a) used a convolutional neural network (CNN) with MODIS TIR radiances to perform cloud mask, COT, CER, and CTH simultaneously; however, like all TIR-only approaches, the method remains limited by reduced sensitivity to optically thick clouds and the non-uniqueness of microphysical signals in thermal radiances (Iwabuchi et al., 2014; Wang et al., 2016a). Zhao et al. (2023) developed a deep-learning ResUnet model using geostationary multispectral brightness temperatures to retrieve COT and CER, along with cloud phase and CTH, achieving improved accuracy for thin to moderately thick clouds, although performance decreases for very thick or spatially heterogeneous cloud fields where TIR sensitivity is limited. Together, these studies highlight substantial progress but also persistent challenges—particularly limited nighttime training data, the narrow swath of lidar-based reference datasets, and the fundamental difficulty of jointly constraining COT and CER from TIR radiances alone—underscoring the need for unified, physically guided ML frameworks capable of consistent day–night cloud microphysical retrievals.

Unlike previous nighttime approaches that relied either on limited two-band information (DNB lunar reflectance and M12 thermal emission), or TIR-only, or were constrained by lidar's sparse spatial sampling, UI-Cloud leverages a broader set of predictors available in both day and night; they include VIIRS thermal emissive bands (M13–M16) and the DNB, allowing a single model to learn radiative–microphysical relationships that remain valid under both solar and lunar illumination and are manifested in multiple bands. The relative contributions of DNB and M13 are further quantified through baseline experiments (Section 4.1), providing physical insight into their complementary roles and highlighting the advantages of the proposed framework over thermal-infrared-only retrieval approaches. A key challenge arises from the 4.065 μm channel (M13), which contains solar contribution during the day (Zhang et al., 2024), disrupting consistency with nighttime thermal-only measurements. To address this, we use the UNified Linearized Vector Radiative Transfer Model (UNL-VRTM, Wang et al., 2014) to construct paired daytime and nighttime lookup tables (LUTs), enabling a physically based correction of daytime M13 solar-residual bias and ensuring that UI-Cloud maintains consistent thermal–microphysical constraints across illumination regimes. UNL-VRTM has been widely applied in satellite-based cloud and aerosol retrievals, including simulation studies for VIIRS, MODIS, and the Ozone Monitoring Instrument (OMI) sensors (Xu et al., 2019; Zhou et al., 2021). For example, Zhou et al. (2021) demonstrated that the model reproduces observed top-of-atmosphere (TOA) reflectance and brightness temperatures (BT) across multiple wavelengths with high accuracy, confirming its suitability for forward modeling and inversion applications.

By combining machine learning with physics-based radiative transfer, UI-Cloud enables stable nighttime retrievals using what is learned from daytime data. With these unified predictors and UNL-VRTM corrections ensuring physical consistency between training and prediction, UI-Cloud retrieves COT and CER globally under both daytime and nighttime conditions, producing physically consistent results that agree with daytime climatology and independent microwave validation. Section 2 describes the datasets, Section 3 details the methodology, Section 4 presents the retrieval results, and Section 5 summarizes the conclusions.

2. Data, data processing, and model

2.1. VIIRS level 1b calibrated products

The VIIRS aboard the Suomi National Polar-orbiting Partnership (S-NPP) satellite provides critical observations for cloud property retrievals across a wide spectral range, spanning visible to thermal infrared wavelengths. VIIRS offers high spatial resolution and global coverage, making it a vital tool for studying clouds, aerosols, and surface properties. The instrument consists of 22 spectral bands, including five Imaging Bands (I-bands) with a resolution of 375 m, sixteen Moderate Resolution Bands (M-bands) at 750 m, and the highly sensitive DNB (Lee et al., 2006), which measures radiances in the 500–900 nm range and is optimized for low-light conditions, enabling nighttime observations (Miller et al., 2013).

VIIRS Level-1b calibrated products (VNP02MOD and VNP02DNB) are used in this study. These data are obtained from the NASA Level-1 Atmospheric Archives and Distribution Systems (LAADS, https://ladsweb.modaps.eosdis.nasa.gov/). They provide radiometrically calibrated and geolocated radiance data, which are then used together with solar zenith angle and satellite viewing geometry information and georeferenced information from VNP03MOD and VNP03DNB, as the one of the inputs for the model training. The calibration of VIIRS radiances is continuously updated to correct known issues, such as stray light contamination in the DNB, ensuring high radiometric accuracy for all observations (Chen et al., 2017).

For this study, thermal emissive bands and the DNB are used to retrieve COT and CER during both daytime and nighttime. The thermal bands offer sensitivity to cloud top temperature, while the DNB measures the moonlight intensity reflected by clouds at nighttime, enabling COT retrievals in the absence of solar illumination. Though M12 (3.693 μm) and M13 (4.065 μm) are thermal emissive bands, both are influenced by solar contributions in the daytime, with M12 showing higher variability and requiring cautious use (Zhang et al., 2024). Therefore, M12 is not used this study.

Because the spectral range (500–900 nm) of the DNB covers the spectral width of VIIRS visible and near-infrared bands that are used for COT retrieval in daytime, and DNB measurements are taken both at day and night, DNB information content for COT remains largely intact between day and night, respectively illuminated by the Sun and the Moon. This consistency serves as a foundation for linking what can be obtained by ML in VIIRS daytime COT retrievals to the night retrievals of COT from DNB. Fig. 1 illustrates the strong correlation between DNB TOA reflectance values and reflectance values from these three M-bands based on nine days of high-quality global data. With correlation coefficients (R) close to 1, the figure demonstrates that DNB TOA reflectance effectively reproduces the radiometric behavior of these daytime channels. This high-level consistency enables the DNB to serve as a physical basis to bridge between daytime and nighttime observations, enabling continuity in COT retrievals across daytime and nighttime conditions, while thermal infrared observations provide the primary constraints for CER retrievals. The details of data selection and filtering criteria are provided in Section 3.2.

2.2. VIIRS cloud properties

The VIIRS Continuity Cloud Properties Version 1 (CLDPROP) Level-2 dataset provides comprehensive cloud optical and microphysical properties, crucial for understanding cloud dynamics and their impact on Earth's radiation budget (Platnick et al., 2019). This dataset includes cloud optical and microphysical parameters such as COT and CER, derived from specific spectral bands optimized for different surface types and atmospheric conditions. COT is primarily retrieved using the M5 (0.67 μm) band for land surfaces and the M7 (0.87 μm) band for ocean surfaces. For snow and ice-covered regions, the M8 (1.24 μm) band is employed, with supplemental retrievals involving the shortwave infrared M10 (1.61 μm) and M11 (2.25 μm) bands, which help to refine the retrieval under challenging surface conditions. These bands provide sensitivity to cloud optical properties, allowing for the differentiation of thin and thick clouds. CER is retrieved during the daytime using a combination of the M10 (1.61 μm), M11 (2.25 μm), and M12 (3.7 μm) bands (Platnick et al., 2020).

At spatial resolution of 750 m, the CLDPROP L2 dataset also provides cloud top properties, including CTH, CTT, and cloud top pressure (CTP) which are critical for understanding cloud vertical structure and its interaction with atmospheric dynamics. There are two cloud phase algorithms in this product, one based on cloud top properties and the other based on optical properties. The cloud top phase (CT) algorithm is sensitive to temperature and altitude, whereas the optical phase (OP) algorithm leverages spectral reflectance to differentiate liquid and ice clouds. During daytime, the OP algorithm is more accurate than the CT algorithm for cloud phase classification, showing better sensitivity to microphysical properties under solar illumination and closer agreement with CALIOP's lidar-based phase identifications (Wang et al., 2020). In addition to cloud phase and cloud top properties, the CLDPROP L2 dataset includes Quality Assurance (QA) flags and uncertainty estimates to ensure retrieval accuracy. These QA flags account for factors such as surface type and cloud phase confidence, providing an indicator of retrieval reliability. Uncertainty estimates associated with COT and CER retrievals further allow the filtering of less reliable data, improving the robustness of the analysis. In this study, only high-quality retrievals with low uncertainty are considered, ensuring that the cloud property estimates are reliable across different environmental conditions.

2.3. Other data

The Modern-Era Retrospective Analysis for Research and Applications, Version 2 (MERRA-2) reanalysis dataset (Gelaro et al., 2017) is used to provide meteorological context and improve the accuracy of cloud property retrievals. Specifically, the MERRA-2 tavg1_2d_slv_Nx (M2T1NXSLV) product is used, which includes single-level diagnostics at a spatial resolution of 0.5° × 0.625° and a temporal resolution of 1 h. This dataset provides essential meteorological parameters, including the 10-m wind components (U10M and V10M) and surface skin temperature (TS). These wind components are critical for understanding the dynamic environment in which clouds form and evolve, particularly over oceanic regions where horizontal advection and shear strongly influence cloud structures. TS provides valuable information about surface–atmosphere energy exchange, affecting cloud formation and stability.

Additionally, cloud liquid water path (LWP) data from the Advanced Microwave Scanning Radiometer 2 (AMSR2) are used as an independent reference for validation. AMSR2 is a passive microwave radiometer onboard the Global Change Observation Mission–Water (GCOM-W1)

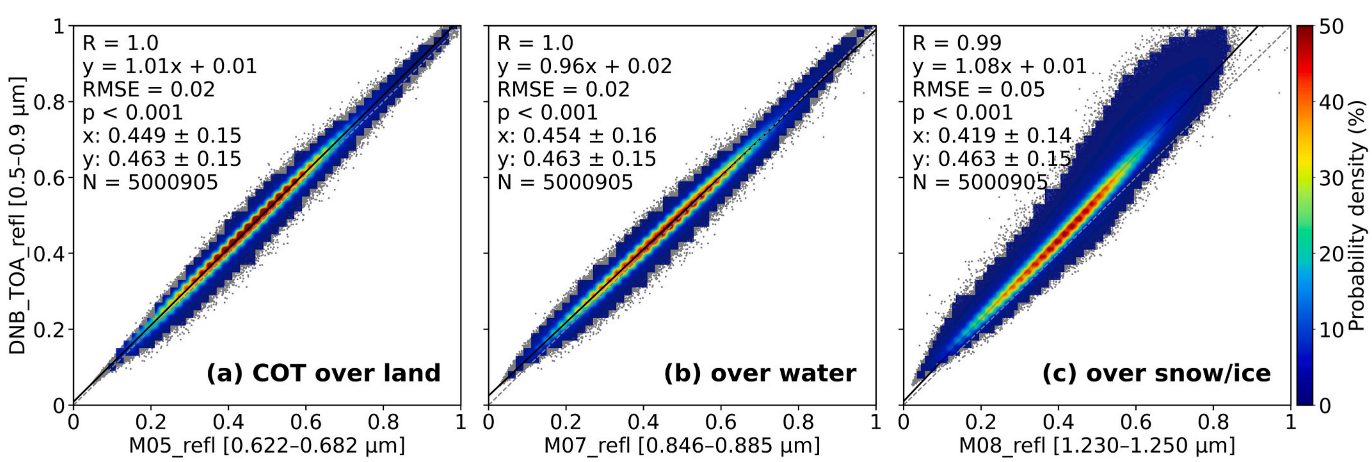

Fig. 1. Scatter plots of 9-day global data, comparing DNB TOA reflectance with VIIRS M-band reflectance used for COT retrieval in the CLDPROP algorithm: (a) M05 (0.67 μm) over land, (b) M07 (0.87 μm) over water, and (c) M08 (1.24 μm) over snow/ice. All data are obtained from VIIRS daytime observations.

satellite, launched by the Japan Aerospace Exploration Agency (JAXA) in 2012. It measures dual-polarized microwave BT at frequencies of 6.9, 7.3, 10.7, 18.7, 23.8, 36.5, and 89.0 GHz, enabling retrievals of key geophysical parameters including cloud LWP, total precipitable water, sea surface temperature, and surface wind speed over the ocean. The AMSR-E/AMSR2 Unified L2B Global Swath Ocean Products, Version 1 (Kummerow et al., 2021) provide global LWP retrievals at an effective spatial resolution of approximately 12–56 km, depending on channel frequency and beam width. Notably, microwave LWP retrievals are known to carry substantial uncertainties, particularly for thin, broken, or non-precipitating liquid clouds, due to beam-filling effects, cloud–rain partitioning, and assumptions about cloud temperature and vertical structure (e.g., Turner et al. (2007)). Nevertheless, microwave measurements are unaffected by solar illumination, allowing continuous day- and nighttime retrievals. The AMSR2 LWP product is collocated with VIIRS-retrieved LWP to evaluate the physical consistency and stability of the nighttime ML retrievals. Details of the LWP validation procedure and evaluation metrics are provided in Section 3.6.

2.4. UNL-VRTM

To support the retrieval of cloud properties under nighttime conditions, this study employs the UNL-VRTM (Wang et al., 2014). The UNL-VRTM (https://unl-vrtm.org, last access: 15 October 2025) is a comprehensive radiative-transfer modeling system that provides physically consistent simulations of radiances and their Jacobians across solar and thermal infrared wavelengths (Xu et al., 2019). The UNL-VRTM consists of seven modules: (1) a vector linearized radiative-transfer solver (Kokhanovsky, 2019; Spurr and Christi, 2019); (2) a linearized Mie-scattering code (Spurr et al., 2012); (3) a linearized T-matrix electromagnetic-scattering code (Spurr et al., 2012); (4) a surface bidirectional reflectance distribution function (BRDF) and bidirectional polarization function (BPDF) module; (5) a Rayleigh-scattering and gas-absorption module based on HITRAN and other molecular databases; and (6–7) two modules for optimal inversion and diagnostic visualization.

In this study, UNL-VRTM is used to generate lookup tables (LUTs) of BT under varying atmospheric and geometric conditions. These LUTs provide a physical basis for correcting nighttime VIIRS BT, particularly for the M13 band, and ensure consistency between daytime and nighttime retrievals (see Section 3.5).

3. Nighttime COT and CER retrieval algorithm

Fig. 2 illustrates the workflow for processing VIIRS data and retrieving nighttime (NT) COT and CER. The procedure involves the following steps:

1) Calculate the DNB TOA reflectance from the VIIRS Level-1b radiance, using solar irradiance for daytime (DT) and lunar irradiance for nighttime (Section 3.1)
2) Assemble training datasets by aggregating radiances and cloud properties to ~6 km resolution and collocating them with MERRA-2 meteorological fields.
3) Select high-quality daytime CLDPROP pixels for training the neural-network (NN) model by applying strict filters: retain only cloudy scenes, separate liquid and ice phases, remove retrievals with COT or CER uncertainties exceeding 25%, and restrict the dataset to ice-free ocean regions (Section 3.2).
4) Train and configure the NN model (multi-task Multi-Layer Perceptron (MLP)) using weighted loss functions and adding 10% random noise (ϵ) to the DNB TOA reflectance during training to consider the uncertainty and enhance robustness under variable illumination (Section 3.3).
5) Prepare nighttime datasets by replacing solar geometry with lunar geometry, applying consistent filtering and feature extraction, and constructing inputs compatible with the daytime-trained model (Section 3.4).
6) Apply nighttime correction with UNL-VRTM lookup tables (LUTs), where BT differences (DT-NT) and scale factors are used to refine nighttime retrievals, yielding final nighttime COT and CER estimates (Section 3.5).
7) Evaluate model performance by comparing predicted COT and CER with reference datasets, assessing correlation coefficients, root mean square error (RMSE), and uncertainty, as shown in Section 3.6. Each of these steps is elaborated upon in the corresponding sections below.

3.1. Obtain the DNB TOA reflectance

The TOA reflectance of the VIIRS DNB is calculated from Level-1b radiances as

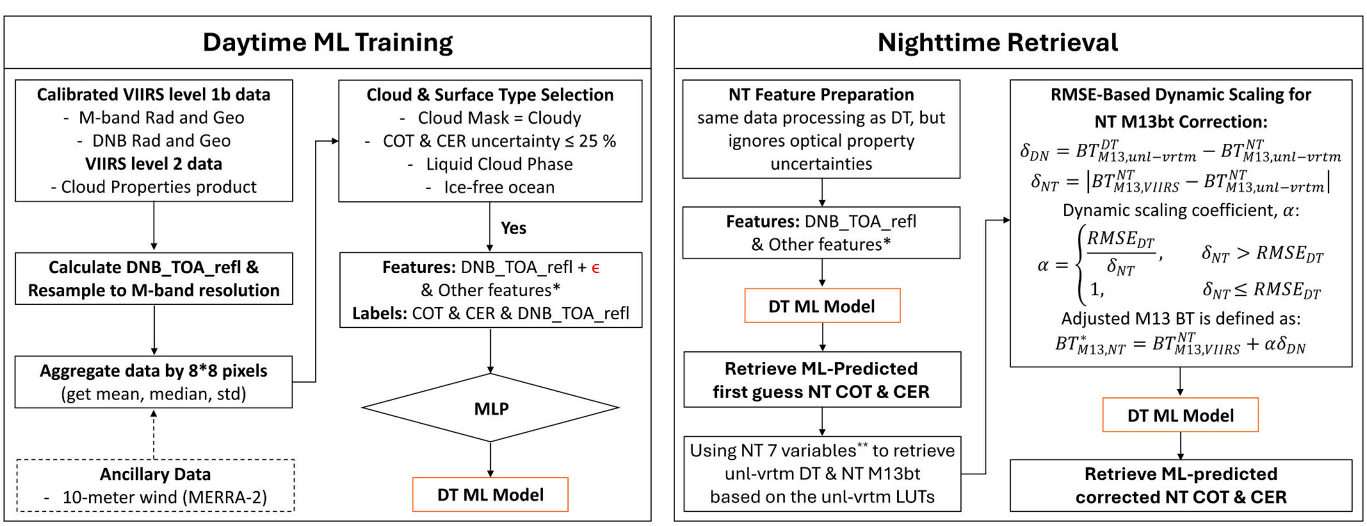

*: Other features including M-band (M13, M14, M15 and M16), geometrics angle (solar zenith, sensor zenith, and scattering angle), cloud top properties (cloud top height, pressure, and temperature), and meteorology data (10-meter wind speed).
**: 7 variables including lunar zenith angle, sensor zenith angle, cloud base/top height, surface temperature, ML-predicted first guess NT COT, and CER.

Fig. 2. Flowchart UI-Cloud, including daytime (DT) ML training and nighttime (NT) retrieval of the COT and CER.

$$\rho_{DNB}^{TOA} = \frac{\pi I_{DNB}}{\mu_0 \int_{\lambda_2}^{\lambda_1} f_{RSR}(\lambda) E_{1AU}^{TOA}(\lambda) d\lambda} \tag{1}$$

where I_{DNB} is the DNB-measured radiance, μ_0 is the cosine of the solar zenith angle, $f_{RSR}(\lambda)$ is the DNB relative spectral response (RSR) at wavelength λ, and $E_{1AU}^{TOA}(\lambda)$ is the spectral irradiance at the top of the atmosphere referenced to 1 AU. The integral ensures consistent spectral weighting across the broadband DNB sensitivity range. The VIIRS DNB is a panchromatic band spanning 342 nm to 1107 nm. The post-launch RSR, obtained from the NOAA STAR Calibration Center online (https://ncc.nesdis.noaa.gov/VIIRS/VIIRSSpectralResponseFunctions.php), provides response curves for 16 detectors over 52 wavelengths (342–1107 nm, total 832 samples). This updated RSR is used to spectrally convolve both solar and lunar irradiance spectra in Eq. (1).

For nighttime conditions, the lunar spectral irradiance $E_{moon}^{TOA}(\lambda)$ is derived from the ROLO Implementation for Moon Observations (RIMO) model, which is based on the RObotic Lunar Observatory (ROLO) reflectance model, with the RIMO Correction Factor (RCF) applied. The ROLO model (Kieffer and Stone, 2005) provides a physics-based lunar disk reflectance derived from more than 38,000 calibrated observations spanning 350–2450 nm, collected over a six-year period. In contrast to the empirical model by Miller and Turner (2009), which employs a simplified photometric function and limited spectral coverage, the ROLO model explicitly accounts for lunar libration, geometric asymmetry, and wavelength-dependent reflectance, offering improved accuracy across varying phase angles and viewing geometries. However, subsequent comparisons with on-orbit lunar observations revealed that the RIMO-derived lunar irradiance tended to underestimate true lunar brightness by approximately 1–14%, particularly at larger phase angles. To correct this bias, the RCF of Román et al. (2020) is applied:

$$RCF(\lambda) = a(\lambda) + b(\lambda)g + c(\lambda)g^2 \tag{2}$$

where g is the moon phase angle and $a(\lambda)$, $b(\lambda)$, $c(\lambda)$ are empirically fitted coefficients at λ wavelength. The corrected lunar spectral irradiance becomes

$$E_{moon,RIMO+RCF}^{TOA}(\lambda) = E_{moon,RIMO}^{TOA}(\lambda) \times RCF(\lambda). \tag{3}$$

This correction improves the accuracy of the modeled lunar irradiance to within $\pm 3\%$ across visible and near-infrared wavelengths (Román et al., 2020). The corrected irradiance is then convolved with the VIIRS DNB RSR to obtain the band-integrated TOA reflectance used in Eq. (1).

Both the Miller and Turner (2009) and RIMO + RCF (Román et al., 2020) models were implemented and compared.

As shown in Fig. S1, the RIMO + RCF approach produces a DNB TOA reflectance distribution that more closely matches daytime observations than the Miller and Turner (2009) model. The Miller approach systematically overestimates nighttime reflectance, resulting in COT retrievals about 7 units higher than those derived using RIMO + RCF. Based on this full-moon comparison, the RIMO + RCF method was adopted for all nighttime reflectance calculations in this study due to its improved consistency with daytime observations.

3.2. *Determination of the suitable pixels for training and validation datasets*

The UI-Cloud daytime (UI-DT-Cloud) process combines VIIRS Level-1b, VIIRS CLDPROP Level-2, and MERRA-2 data to construct a high-quality dataset for ML applications. The focus is on ice-free ocean regions where cloud detection confidence is high, and retrieval uncertainties are minimized. High QA data are essential to ensure that the training dataset is reliable, representative, and free from significant noise and biases, ultimately improving model performance.

The final dataset prepared for model training integrates the following carefully selected features: DNB TOA reflectance, BT from VIIRS M-bands (M13, M14, M15, and M16), geometric angles (solar zenith, sensor zenith, and scattering angle), cloud-top properties (cloud-top height, pressure, and temperature), and 10-m wind speed from MERRA-2. The primary labels include COT, CER, and DNB TOA reflectance. In the ML training framework, DNB TOA reflectance plays a dual role: it is used as an input feature (with a 10% noise perturbation added for robustness) and is also included as an output label, allowing the model to learn a physically consistent mapping between DNB reflectance, thermal radiances, and cloud microphysical properties.

The VIIRS Level-1b and Level-2 datasets, including VNP02MOD, VNP03MOD, VNP02DNB, VNP03DNB, and CLDPROP_L2, provide the core cloud parameters and geometric information needed to build the dataset. These cloud-related measurements are further supplemented by 10-m wind components from MERRA-2 reanalysis data. The DNB TOA reflectance is resampled to match the M-band resolution, after which the data are aggregated over an 8×8 pixel grid (each pixel is 750 m), resulting in a final resolution of 6 km. Aggregation can reduce random noise, smooth outliers, and lower the mean bias in ML predictions, which enhances model accuracy. The final aggregated dataset contains parameters, with mean, median, and standard deviation values calculated for each 8×8 pixel grid. Additionally, glint angles are calculated, and pixels with glint angles below 40 degrees are excluded to reduce the impact of sun-glint (Levy et al., 2003). MERRA-2 data are integrated to provide meteorological context. Specifically, the closest-in-time U10M and V10M wind components from MERRA-2 are resampled to match the VIIRS M-band grid using bilinear interpolation. Wind speed (WS10M) is calculated from these components and added to the dataset, offering important insights into wind conditions relevant to cloud formation and dynamics.

The determination of cloud phase in the dataset relies on both cloud top properties and optical properties. To ensure the accuracy of the training data, cloud masking and quality control steps are implemented using the Cloud Mask product from CLDPROP_L2. Only pixels flagged as "Cloudy" are retained, while those with uncertain classifications are discarded to prevent biases. Additionally, pixels with high uncertainties (greater than 25% for either COT or CER) are filtered out. This strict quality control ensures that only reliable retrievals with low uncertainty are included, contributing to the robustness of the dataset. Further filtering based on surface type ensures that the dataset focuses on ice-free ocean regions. Ice-free ocean pixels are identified using the "Earth surface type used in optical thickness retrieval" flag in the CLDPROP_L2 Quality Assurance (QA) field, which incorporates ancillary snow and ice information, including the Near-real-time Ice and Snow Extent (NISE) dataset. Over ice-covered seas, reflectance values tend to have high uncertainty due to the complex surface properties, making them less reliable for cloud property retrievals (Platnick et al., 2019). This step enhances the homogeneity of the data and ensures consistency in surface type for downstream ML applications.

To capture representative variability while maintaining computational efficiency, nine days of daytime global data (29 August – 6 September 2020) were selected, corresponding to four days before the full moon, the full-moon day (2 September 2020), and four days after. This temporal window captures representative daily variability and aligns with the lunar cycle used in the nighttime analysis, ensuring temporal consistency between the daytime training and nighttime application periods. Because the total dataset, consisting of 13,177,251 liquid-cloud samples, is extremely large, a probability-density-function (PDF)-preserving downsampling method is applied to reduce data volume while retaining the original statistical distribution of COT. Samples are randomly selected in proportion to their occurrence frequency in the full dataset, ensuring that the downsampled data maintain the natural variability and relative frequency of both optically thin and thick clouds. The final dataset contains 5,000,905 samples, providing a statistically representative and computationally manageable dataset suitable for model training, validation, and testing.

3.3. Neural Network (NN) model training and configuration for UI-DT-Cloud

The NN model developed in this study is a MLP implemented in PyTorch and trained using PyTorch Lightning. It is designed to retrieve cloud optical and microphysical parameters from VIIRS observations through a multi-task learning framework that enables the simultaneous prediction of COT, CER, and DNB TOA reflectance using the input features described in Section 3.2. Weighted loss functions are applied to balance the learning of these three physically related quantities.

The MLP architecture consists of an input layer, nine hidden layers, and an output layer. Each hidden layer performs a linear transformation followed by batch normalization, Leaky ReLU activation, and a dropout rate of 0.025 to prevent overfitting. Hyperparameter tuning determined the optimal configuration, with the maximum hidden-layer dimension reaching 2048 neurons in the central layer. This depth and width allow the model to capture complex nonlinear relationships among radiative and atmospheric predictors.

All input features are normalized using a Box–Cox transformation followed by z-score normalization to enhance numerical stability and convergence. This preprocessing step reduces distribution skewness and improves the representation of sparsely populated regions of the data during model training. To improve robustness to nighttime DNB uncertainty, DNB TOA reflectance is included as both an input feature and an auxiliary output label. Because the model is trained using daytime DNB reflectance but applied to nighttime lunar-illuminated observations, additional uncertainties may be introduced in the DNB signal. To account for these uncertainties, 10% random noise (ϵ) is added to the DNB input during training while the model is simultaneously required to reproduce the original DNB reflectance. This strategy encourages the ML model to learn and tolerate a much noisier feature of DNB, thereby improving the robustness of cloud-property retrievals under varying illumination conditions; hence, it can be readily applied at nighttime for COT and CER retrievals.

The training dataset, derived from daytime COT and CER retrievals, is randomly split into 70% for training, 20% for validation, and 10% for testing. A weighted mean squared error (MSE) loss function is adopted:

$$L_{\text{total}} = w_{\text{COT}} \bullet L_{\text{COT}} + w_{\text{CER}} \bullet L_{\text{CER}} + w_{\text{DNB}} \bullet L_{\text{DNB}}, \tag{4}$$

where $w_{\text{COT}} = 0.5$, $w_{\text{CER}} = 0.5$, and $w_{\text{DNB}} = 1.0$. Optimization is performed using Stochastic Gradient Descent (SGD) with a learning rate of 0.05 and momentum of 0.9. Training proceeds for a maximum of 500 epochs with a batch size of 50,000 samples to ensure statistical stability for the global dataset.

The model minimizes the weighted MSE during training, while evaluation performance is assessed using the coefficient of determination (R^2), RMSE, mean absolute error (MAE), and mean bias, computed separately for each output and averaged across epochs. This configuration ensures efficient large-scale training while maintaining robustness and interpretability across multiple retrieval targets.

3.4. UI-Cloud Nighttime (UI-NT-Cloud): dataset preparation for retrieval

The preparation of the nighttime dataset follows a similar process to the daytime training data described in Section 3.2, with several adjustments to accommodate nighttime conditions. For nighttime data, lunar zenith and azimuth angles replace solar angles to account for the lunar illumination. Additionally, cloud phase determination relies solely on cloud top properties in the infrared spectrum. To maintain consistency with the daytime training configuration, the analysis focuses on liquid-phase clouds over ice-free ocean regions at night. The feature set for the nighttime remains the same as that of the daytime training dataset, with a final output resolution of 6 km.

3.5. Creation of UNL-VRTM LUTs for Nighttime M13 BT correction

Daytime VIIRS thermal emissive bands (TEBs), particularly M12 (3.693 μm) and M13 (4.065 μm), are affected by solar contributions that do not influence nighttime measurements. However, M12 exhibits higher variability and greater calibration uncertainty (Zhang et al., 2024), and is therefore excluded from this study. While M13 provides more stable measurements, its residual solar contamination during the day introduces a systematic bias when applying daytime-trained models to nighttime conditions. To address this, we employ the UNL-VRTM (Section 2.4) to construct physics-based LUTs that bridge the daytime–nighttime gap. The spectral range used in these simulations follows the VIIRS M13 band, with spectrum from 3850 to 4250 nm.

The LUTs are generated by simulating M13 BT under both daytime (solar + thermal) and nighttime (thermal only) conditions. Each LUT is parameterized by seven key variables: solar/lunar zenith angle (SZA/LZA), viewing zenith angle (VZA), cloud base height (CBH), CTH, TS, COT, and CER. The final LUTs resolution are SZA = 0°–80° (5°), VZA = 0°–80° (5°), CBH = 0–9 km (1 km), CTH = 0.5–10 km (1 km), TS = 265–310 K (5 K), COT = 0–80 (1), and CER = 4–30 μm (1 μm). CBH is estimated following the regression-based approach of Noh et al. (2017), which relates cloud water path (CWP) and CTH.

Because atmospheric temperature profiles strongly affect thermal emission and BT simulations, we incorporate both standard UNL-VRTM profiles (tropical, mid-latitude summer/winter, high-latitude summer/winter) and three additional MERRA-2 latitude-dependent profiles (40–60°S, 60–70°S, 70–90°S) to improve the representation of atmospheric temperature structures over the southern high latitudes. To best represent real-world conditions, a 5° latitude-based weighting scheme is applied: pressure-weighted non-negative least squares (NNLS) fitting combines profiles within each latitude band, with a constraint to switch to the single profile closest to observed surface temperature if differences exceed 5 K. For each pixel, the corresponding profile weights are determined from its 5° latitude band. Rather than selecting a single atmospheric-profile LUT, the simulated M13 BT is calculated as a weighted combination of the eight atmospheric-profile LUTs:

$$M13BT_{weighted} = \sum\nolimits_{i=1}^{8} w_i \times M13BT_i, \tag{5}$$

where $M13BT_i$ is the interpolated BT from LUT i, and w_i is the latitude-dependent profile weight derived from the pressure-weighted NNLS fitting procedure. This approach allows multiple atmospheric profiles to contribute to the retrieval according to latitude-dependent weights, providing smooth transitions between climate regimes. This blending ensures improved consistency between modeled and observed BTs.

In total, eight LUTs (five using atmospheric profiles already in UNL-VRTM and three derived from MERRA-2 as inputs for UNL-VRTM) are constructed for both daytime and nighttime conditions, convolved with the M13 RSR function. These LUTs provide paired daytime and nighttime BT simulations across the parameter space, enabling the derivation of the physical day-night offset

$$\delta_{DN} = BT^{DT}_{M13,UNL-VRTM} - BT^{NT}_{M13,UNL-VRTM}, \tag{6}$$

and the nighttime observation-simulation mismatch

$$\delta_{NT} = \left| BT^{NT}_{M13,VIIRS} - BT^{NT}_{M13,UNL-VRTM} \right|. \tag{7}$$

A dynamic scaling coefficient α is then defined using an RMSE-based rule:

$$\alpha = \begin{cases} \dfrac{RMSE_{DT}}{\delta_{NT}}, \delta_{NT} > RMSE_{DT}, \\ 1, \delta_{NT} \le RMSE_{DT}, \end{cases} \tag{8}$$

where $RMSE_{DT}$ is obtained from daytime validation. The purpose of α is to prevent overcorrection when the UNL-VRTM nighttime simulation deviates substantially from the observed nighttime M13 BT. In such cases, the correction magnitude is reduced according to the model–observation discrepancy, thereby limiting the propagation of radiative-transfer uncertainties into the final nighttime retrievals.

For each nighttime pixel:

1. First-guess COT and CER are obtained from the ML model.
2. The corresponding M13 BT is retrieved from the nighttime LUTs using the geometric and cloud parameters of the pixel, including the first-guess COT and CER.
3. The observed–simulated difference (δ_{NT}) is computed, and the corresponding scale coefficient α is determined using the RMSE-based rule. With these terms, an adjusted M13 BT is defined as

$$BT^{*}_{M13,NT} = BT^{NT}_{M13,VIIRS} + \alpha\delta_{DN}, \tag{9}$$

which represents the day–night–bridged BT used as the correction target for updating nighttime COT and CER.

4. The corrected COT and CER are obtained by adjusting the ML first guess using this LUT-based correction

This single-step $\alpha \times \delta_{DN}$ framework combines ML retrievals with UNL-VRTM physics, reducing M13 solar residual biases and yielding more accurate nighttime COT and CER estimates.

3.6. ML-cloud evaluation

The performance of the ML models is first assessed under daytime conditions, where high-quality reference retrievals of COT and CER are available from the VIIRS CLDPROP L2 product. The ML outputs are compared against CLDPROP at the aggregated 6 km resolution, and evaluation metrics including the coefficient of determination (R^2), RMSE, MAE, and mean bias are reported. These daytime evaluations provide the benchmark accuracy and generalization capability of the model.

For nighttime retrievals, their validation relies on indirect measures and consistency checks. For liquid clouds, an independent consistent check is made through comparison of LWP with AMSR2 measurements. LWP can be calculated from the COT and CER following the definition of Stephens (1978):

$$LWP = \frac{4 \bullet COT \bullet CER \bullet \rho}{3Q} \tag{10}$$

where ρ is the density of liquid water (assumed to be 1 g cm^{-3}) and Q is the extinction cross-section efficiency, approximated as 2 for visible wavelengths. LWP is expressed in g m^{-2} after appropriate unit conversion.

Unlike solar-based sensors, microwave instruments such as AMSR2 can retrieve LWP continuously under both day and night conditions, as microwave radiation is not affected by solar illumination and can penetrate cloud layers. These characteristics make AMSR2 an ideal independent dataset for evaluating UI-NT-Cloud retrievals. The UI-Cloud LWP is collocated with AMSR2 LWP retrievals over ocean, and validation metrics (R^2, RMSE, MAE, and bias) are computed to assess physical consistency and retrieval robustness.

4. Retrieval demonstration and discussion

This section evaluates the performance of the UI-Cloud retrieval framework and its ML extension to nighttime conditions. We first assess the model's accuracy using daytime VIIRS CLDPROP L2 retrievals as reference (Section 4.1) and interpret the feature contributions through SHapley Additive exPlanations (SHAP) analysis. Next, we describe the development and application of the UNL-VRTM-based correction to address solar-residual effects in the M13 band (Section 4.2). The corrected nighttime inputs are then used to generate and validate nighttime COT and CER retrievals through comparisons with VIIRS daytime observations and AMSR2 LWP measurements. Finally, we evaluate the model's robustness under varying lunar illumination fractions to determine the practical limits of nighttime applicability (Section 4.3).

4.1. UI-DT-Cloud ML performance

The overall model performance for daytime retrievals is shown in Fig. 3, with additional training results provided in Fig. S2. The ML-predicted COT and CER closely match the VIIRS CLDPROP L2 observations across the training, validation, and test subsets, exhibiting consistently high correlations ($R = 0.98$) and low RMSE values (≈ 2.8 for COT and ≈ 0.9 μm for CER). The blind test dataset, which was not used during training or hyperparameter tuning, serves to independently evaluate the model's generalization to unseen conditions. Regression slopes near unity and negligible mean biases demonstrate the strong generalization capability of the model across diverse cloud regimes and viewing geometries. In addition to COT and CER, the model also predicts DNB TOA reflectance as an auxiliary label. Although not a direct cloud property, this variable was incorporated with a 10% random-noise perturbation during training to enhance the network's denoising robustness and stabilize its performance under varying illumination conditions. The model reproduced DNB TOA reflectance nearly perfectly ($R = 1.0$, RMSE $= 0.01$), confirming the reliability of this feature as a consistent radiometric constraint.

To further evaluate the roles of DNB and M13 (4.05 μm) in the retrieval framework, two additional baseline experiments were conducted using the independent testing dataset (Fig. S3). The first baseline excludes M13 and uses only DNB together with longwave infrared channels (M14–M16, 8.55, 10.763, 12.013 μm), while the second baseline excludes both DNB and M13 and relies solely on thermal infrared observations (M14–M16). The results show that DNB provides the primary constraint for COT retrieval, whereas M13 contributes substantially to CER retrieval. When DNB is removed, the COT correlation decreases from 0.98 to 0.83 and the RMSE increases from 2.88 to 7.34. In contrast, CER retrieval degrades when M13 is excluded, with the correlation decreasing from 0.98 to 0.95 and the RMSE increasing from 0.93 to 1.54 μm. The substantially poorer performance of the TIR-only configuration further demonstrates the complementary roles of DNB and M13 and highlights the benefits of combining visible/lunar-reflectance and thermal-infrared observations within a unified retrieval framework.

To interpret the physical relevance of the predictors, we applied SHapley Additive exPlanations (SHAP; Lundberg and Lee (2017)), a game-theoretic feature-attribution method that quantifies the contribution of each input feature to the model output. SHAP values were computed using the DeepExplainer framework, which is specifically designed for neural-network models, with 1000 randomly sampled background points from the training dataset to ensure stable and representative feature attributions. Fig. 4 shows that, for COT retrievals, the DNB TOA reflectance and thermal brightness temperatures (especially M15 and M13) dominate the model sensitivity, together explaining over 30% of the total contribution. The DNB effectively replaces traditional visible-band inputs by capturing moonlight and daylight reflectance in a unified radiometric framework, enabling consistent retrievals across both daytime and nighttime conditions. The geometric parameters—solar zenith angle, sensor zenith angle, and scattering angle—also provide meaningful input for angular-dependent reflectance corrections.

For CER, the model relies primarily on TIR bands M13–M16, consistent with the strong sensitivity of thermal infrared observations to cloud particle size. The SHAP analysis reveals distinct sign patterns among the thermal channels. For example, lower M13 (4.05 μm) and M16 (12.013 μm) BTs generally contribute positively to the retrieved

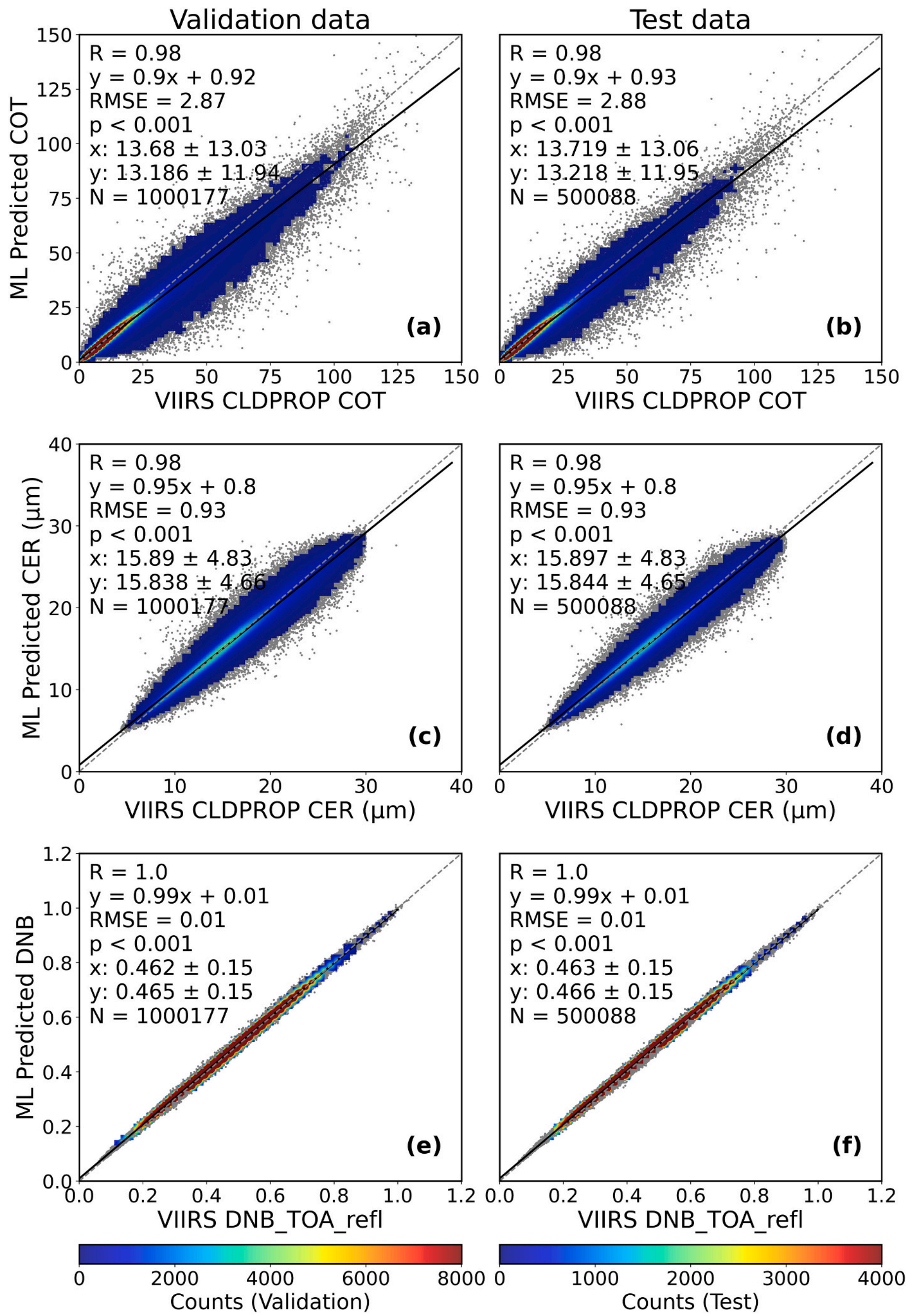

Fig. 3. Comparison between ML-predicted and VIIRS observations for (a, b) COT, (c, d) CER, and (e, f) DNB TOA reflectance, shown for the (a, c, e) validation and (b, d, f) testing datasets.

CER, whereas M14 (8.55 μm) and M15 (10.763 μm) exhibit the opposite tendency. To further provide physical context for these band-dependent SHAP patterns, representative daytime UNL-VRTM simulations were conducted using a mid-latitude summer atmosphere (Fig. S4). The simulated CER Jacobians ($\partial BT/\partial CER$) show distinct spectral and state-dependent responses. M13 exhibits predominantly negative sensitivity over moderate-to-large COT and CER, with positive sensitivity occurring mainly at smaller COT and CER. M14 is predominantly positive except at smaller CER, while M15 shows generally weak positive sensitivity except for stronger negative sensitivity under low-COT conditions. M16 exhibits predominantly negative sensitivity, with only weak positive responses under some conditions. These distinct radiative responses provide additional physical context for interpreting the different SHAP patterns among M13–M16. Because SHAP values represent feature attributions within the multivariate neural network (that are nonlinear and are designed to perform well for different COT and CER cases) rather than direct radiative Jacobians (that are valid for a given set of COT and CER values), their signs are not expected to correspond one-to-one with $\partial BT/\partial CER$. Nevertheless, consistent the Jacobian analysis for the limited cases (in Fig. S4), SHAP (Fig. 4) shows that M14 overall has the positive sensitivity while M13 has the negative sensitivity to the change of COT and CER. More importantly, the SHAP ranking shows that M13–M16 collectively dominate the CER retrieval, accounting for more than 65% of the total feature contribution, whereas DNB TOA reflectance contributes less than 1%. This result indicates that CER retrieval is primarily constrained by thermal infrared information, with DNB TOA reflectance playing only a minor role. Together, these SHAP patterns suggest that the ML model captures physically meaningful radiative information

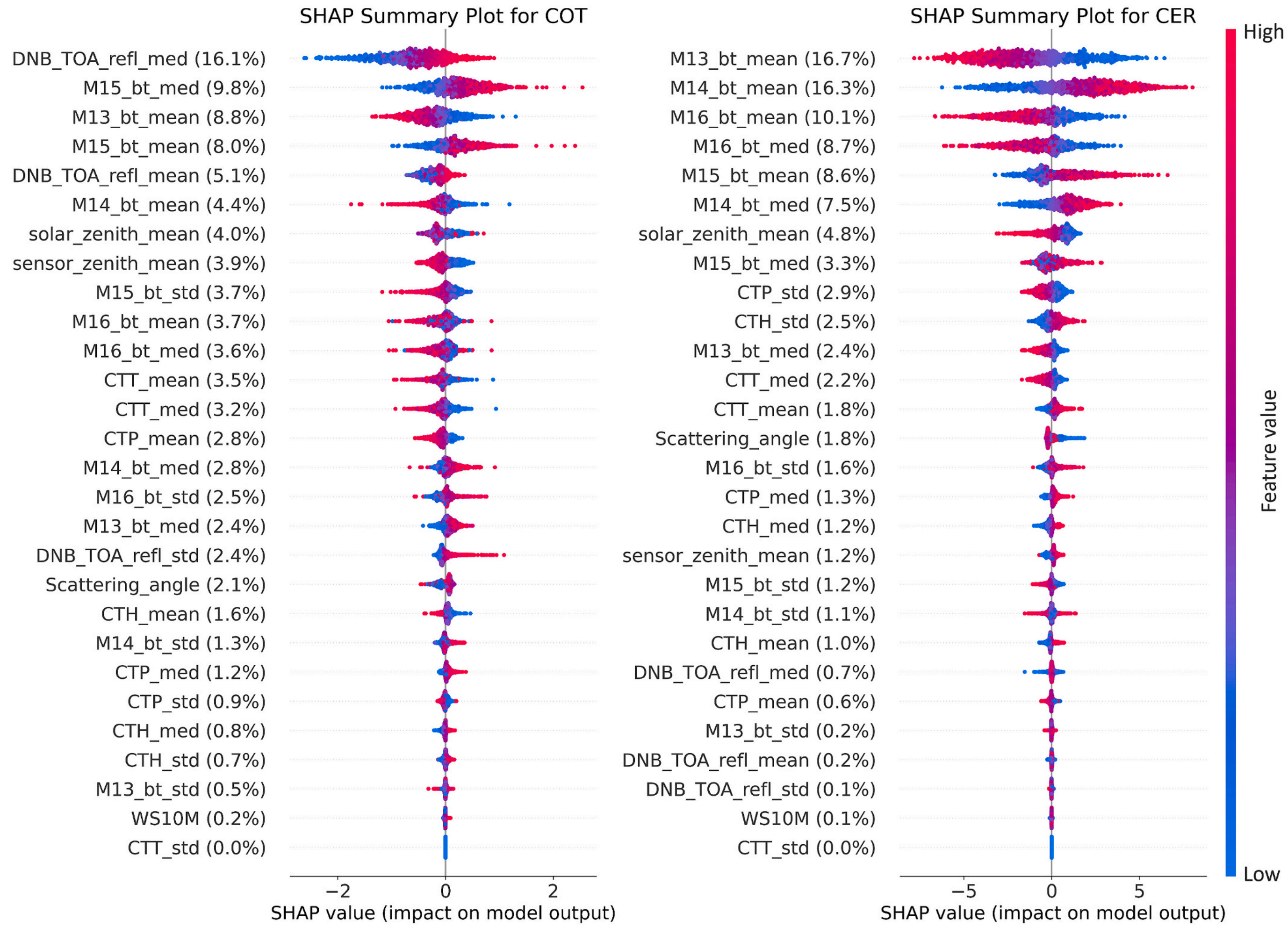

Fig. 4. SHAP summary plots features for predicting COT (left) and CER (right) showing the relative importance of input. Note: VIIRS thermal emissive bands — M13 (3.973–4.128 μm), M14 (8.4–8.7 μm), M15 (10.263–11.263 μm), and M16 (11.538–12.488 μm).

while exploiting complementary relationships among multiple TIR channels.

Fig. 5 shows the spatial validation on 12 September 2020, a date excluded from the training period, confirms that the ML retrievals accurately reproduce the global daytime distribution of liquid clouds. The predicted COT and CER fields exhibit strong spatial agreement with VIIRS CLDPROP L2, capturing enhanced COT in midlatitude storm-track regions and larger CER in subtropical marine stratocumulus decks. Quantitatively, the global comparison yields $R = 0.96$, bias $= 0.39$, RMSE $= 3.68$, and relative bias $= 6.46\%$ for COT, and $R = 0.96$, bias $= -0.10$ μm, RMSE $= 1.46$ μm, and relative bias $= 0.16\%$ for CER. Over 80% of COT differences within ± 2 and 80% of CER differences within ± 1 μm. These statistics indicate close consistency across most regions, with larger deviations primarily near cloud edges or in areas with optically thin clouds. This strong agreement demonstrates that the daytime model provides a reliable and physically robust baseline for subsequent nighttime applications.

4.2. *Day–night radiometric consistency and UNL-VRTM-based M13 BT correction*

To extend the daytime-trained ML model to nighttime conditions, the geometric and radiometric inputs were adjusted to ensure consistency between solar- and lunar-illumination regimes. Specifically, the SZA in daytime data was replaced with the LZA for nighttime retrievals, while other parameters—viewing geometry, surface temperature, and thermal brightness temperatures—were retained. To ensure high data quality and avoid excessive uncertainties under dim illumination, only nighttime pixels with LZA $\leq 60°$ were used in this analysis.

Fig. 6 compares the distributions of key input features between the daytime and nighttime datasets. The datasets include nine days of global daytime training data (four days before and after the full moon, plus the full moon day) and one day of nighttime full moon observations, providing a consistent temporal and geometric context for comparison. Overall, the feature distributions are remarkably similar, demonstrating that the nighttime predictor space lies well within the daytime-trained domain—a crucial condition for ensuring the transferability of the ML model. This similarity indicates that the model can effectively generalize its learned physical relationships from solar-illuminated scenes to moonlit conditions without requiring major architectural changes.

However, a notable difference appears in the M13 (4.065 μm) BT, which exhibits an average bias of 7.69 K between daytime and nighttime observations. This offset primarily originates from solar residuals in the M13 band during daytime. The magnitude of solar contamination in M13 overall depends on several factors including: under clear-sky conditions, the M13 daytime–nighttime difference is relatively small ($\approx$1.3 K) (not shown here), but it increases significantly (6–8 K) when clouds are present due to enhanced multiple scattering and reflection within the cloud layer. This leads to the day-night radiometric inconsistency in M13 that can propagate into cloud property retrievals, especially for CER, for which M13 is one of the most influential predictors (Fig. 4). There, solar contamination requires explicit correction

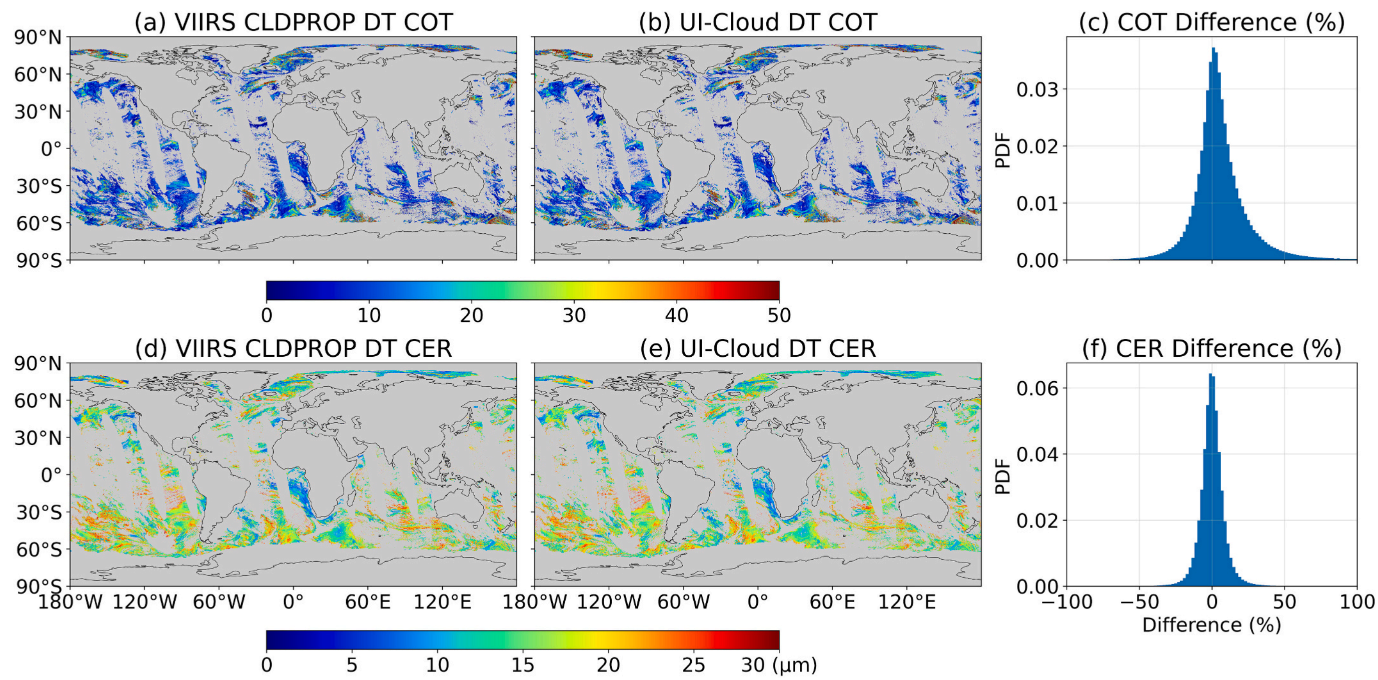

Fig. 5. Global distributions of (a–c) COT and (d–f) CER on 12 September 2020. Panels (a, d) show VIIRS CLDPROP L2 retrievals, panels (b, e) show ML-predicted values, and panels (c, f) show the probability density distribution (PDF) of their percentage differences.

for applying UI-DT-Could to UI-NT-Cloud. To address this issue, UNL-VRTM is used to simulate BT under both daytime (solar + thermal) and nighttime (thermal-only) conditions, and create the LUT for removal of solar contamination in M13. Each LUT is parameterized by seven key variables—SZA/LZA, VZA, CBH, CTH, TS, COT, and CER, as described in Section 3.5.

Fig. 7 illustrates the comparison between VIIRS M13 BT and UNL-VRTM simulations using the nine-day daytime training dataset. Panel (a) shows the scatter-density relationship between VIIRS observations and UNL-VRTM daytime simulations, yielding a strong correlation ($R = 0.91$) and an RMSE of 4.25 K, demonstrating that the LUTs reproduce observed daytime radiances with high fidelity. Panel (b) presents the PDF distribution of VIIRS and UNL-VRTM daytime simulations, showing close agreement with a mean bias <0.1 K, confirming the model's reliability under solar-illuminated conditions. Panel (c) compares UNL-VRTM daytime and nighttime simulations, where we assume identical cloud properties for both cases (the same daytime dataset is used to generate nighttime simulations). Under this assumption, the model predicts an average 13.36 K decrease in M13 BT from day to night, larger than the 7.69 K difference observed in Fig. 6. This overestimation may arise partly from diurnal variations in cloud microphysics, such as changes in phase composition, vertical structure, or emissivity, which are not represented in the simulation. Consequently, the modeled offset represents a theoretical radiative difference due to the transition from solar + thermal to thermal-only conditions.

To illustrate the nighttime M13 BT correction, Supplementary Fig. S5 shows a comparison of VIIRS daytime/nighttime observations with the UNL-VRTM nighttime–adjusted simulations. For each nighttime pixel, the difference between the VIIRS-observed nighttime M13 BT and the UNL-VRTM nighttime simulation (δ_{NT}) is first calculated using the same seven parameters—LZA, VZA, CBH, CTH, TS, COT, and CER—with COT and CER provided by the UI-Cloud ML-predicted nighttime first-guess retrievals, as defined in Eq. (7). This δ_{NT} value quantifies how closely the radiative-transfer simulation reproduces the observed BT and therefore indicates the confidence level of the UNL-VRTM result. If $\delta_{NT} \leq 5$ K (the RMSE threshold determined from the daytime validation in Fig. 7a), the nighttime simulation is considered reliable, and the difference between UNL-VRTM daytime and nighttime simulations is directly used to correct the solar-residual bias in the observed M13 BT. Conversely, if $\delta_{NT} > 5$ K, the model–observation discrepancy indicates lower confidence, and a dynamic scaling factor (defined in Eq. (8) in Section 3.5) is applied to reduce the correction magnitude accordingly. The 5 K threshold thus represents the level of radiometric consistency at which the model's correction can be trusted.

After this conditional correction is applied, the adjusted nighttime M13 BT distribution aligns closely with the daytime VIIRS distribution (Fig. S5), demonstrating that the UNL-VRTM-based correction method effectively mitigates solar-residual effects and provides a consistent thermal baseline for subsequent nighttime COT and CER retrievals.

4.3. UI-NT-cloud COT and CER retrieval performance and validation

Building upon the M13 BT correction described in Section 4.2, the adjusted nighttime inputs were used to retrieve nighttime global COT and CER on 2 September 2020, corresponding to a full-moon night. In this section, we first compare the initial ("first-guess") nighttime retrievals with those after the UNL-VRTM-based correction to assess how effectively the correction mitigates residual solar contamination and restores radiometric consistency. The analysis then evaluates the ML results against independent AMSR2 LWP observations to validate the physical accuracy of the retrieved cloud properties.

Fig. 8 presents the global distributions of nighttime COT and CER retrieved by the ML model before and after the UNL-VRTM-based correction on 2 September 2020 (full-moon night). The initial uncorrected ("first guess") retrievals generally reproduce the large-scale spatial patterns of daytime VIIRS CLDPROP L2 data, but they exhibit systematic biases—COT tends to be slightly higher, while CER is strongly overestimated over marine stratocumulus regions, frequently exceeding 30 μm. This CER bias arises because, without solar contribution, the nighttime M13 BT is lower than its daytime value; since M13 BT is inversely related to CER, a cooler M13 signal leads the model to infer unrealistically large particle sizes. After applying the UNL-VRTM-based correction, both COT and CER fields become physically consistent with the daytime benchmarks, and CER values fall within a realistic range (< 30 μm).

Fig. 9 shows the PDFs of daytime VIIRS observations, ML retrievals,

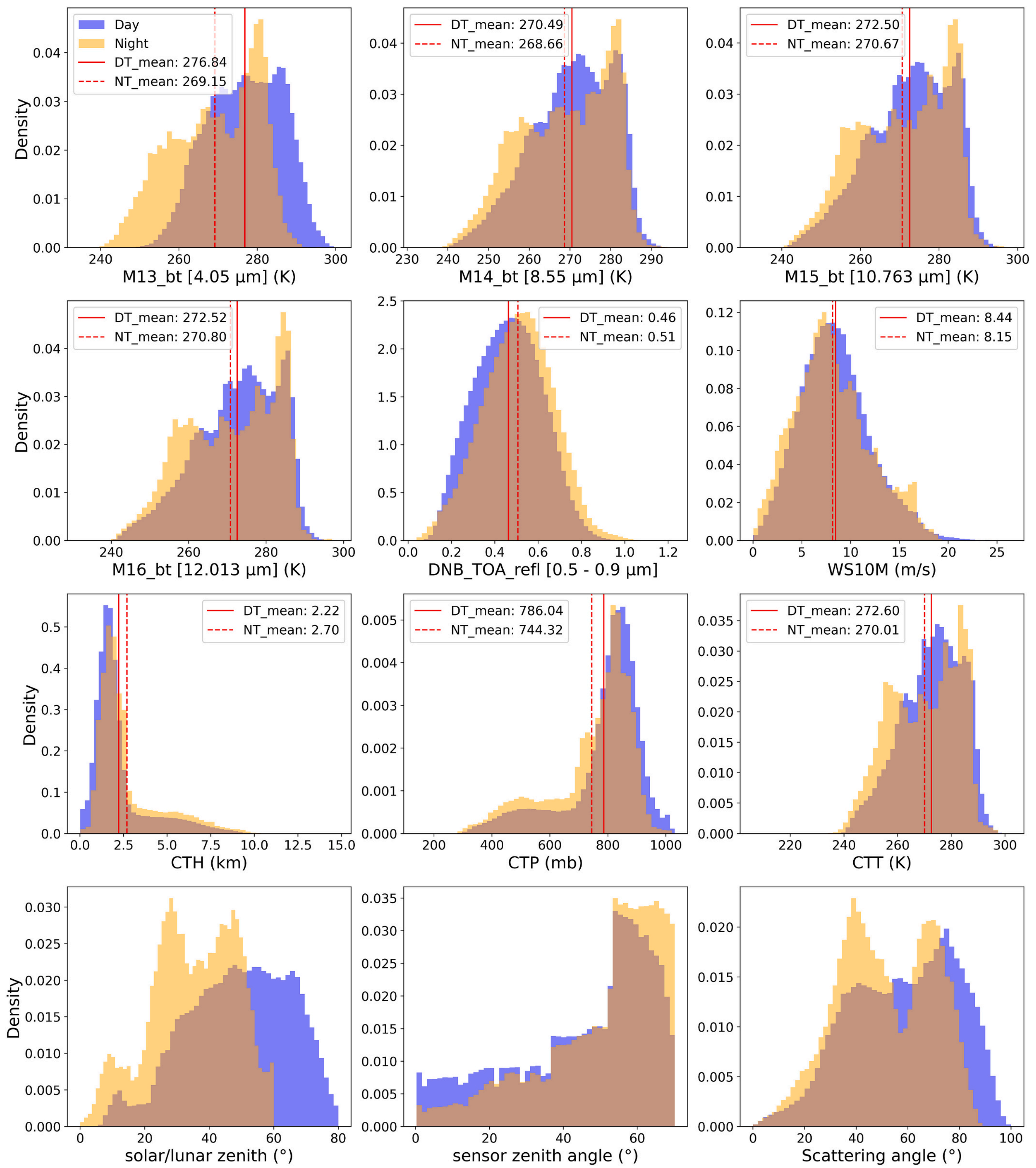

Fig. 6. Comparison of key input variables between daytime 9-day training data (blue) and nighttime 1-day (2020/9/2) global data (orange) for liquid clouds. Panels show the distributions of M13–M16 brightness temperatures (BT), DNB TOA reflectance, 10 m wind speed, cloud top height/pressure/temperature, solar/lunar zenith angle, sensor zenith angle, and scattering angle. Solid red lines denote the daytime mean values, and dashed red lines indicate the nighttime mean values. (For interpretation of the references to colour in this figure legend, the reader is referred to the web version of this article.)

and nighttime ML retrievals for COT and CER, both before and after the UNL-VRTM-based M13 BT correction. The daytime ML retrievals show nearly identical PDF shapes and mean values to the VIIRS daytime observations, indicating that the model maintains consistency with the daytime reference. In the first-guess results, the nighttime COT and CER distributions deviate from the daytime reference, with mean values of 15.7 and 27.2 μm, respectively, compared with 14.6 and 15.9 μm during the day. The CER distribution is especially biased toward unrealistically

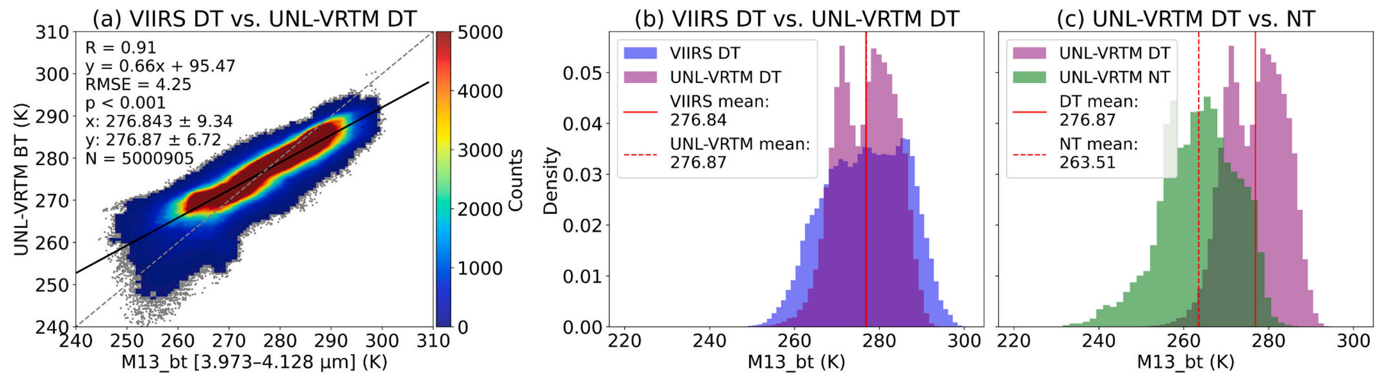

Fig. 7. Comparison between VIIRS and UNL-VRTM M13 BT based on the 9-day daytime training dataset. (a) Scatter-density plot comparing VIIRS observed and UNL-VRTM-simulated daytime M13 BT. (b) Distribution comparison between VIIRS and UNL-VRTM daytime simulations; the red solid and dashed lines indicate the mean BT values from VIIRS and UNL-VRTM daytime simulations, respectively. (c) Distribution comparison between UNL-VRTM daytime and nighttime simulations; the red solid and dashed lines represent the mean BT values for UNL-VRTM daytime and nighttime simulations, respectively. (For interpretation of the references to colour in this figure legend, the reader is referred to the web version of this article.)

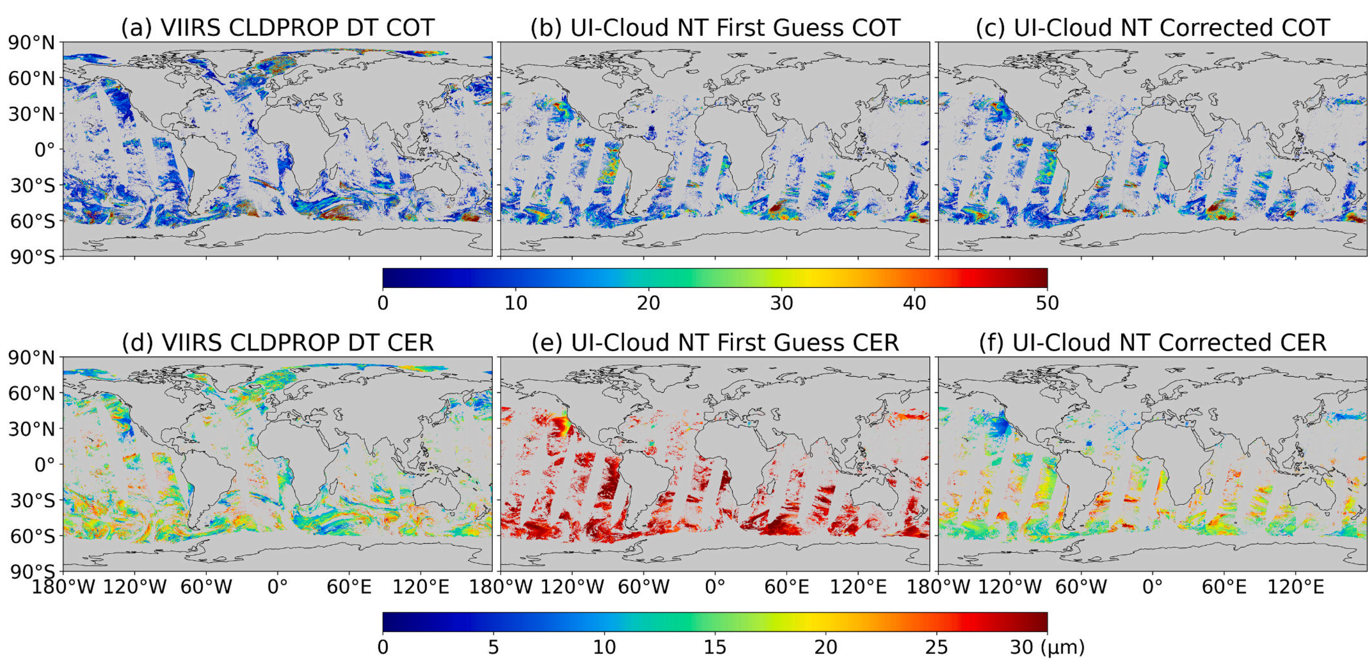

Fig. 8. Global distribution of COT (a-c) and CER (d-f) on 2 September 2020. (a, d) VIIRS CLDPROP L2 daytime reference; (b, e) initial nighttime ML predictions; (c, f) corrected nighttime ML retrievals after applying UNL-VRTM-based BT adjustments.

large values (> 30 μm) because the nighttime M13 BT is cooler in the absence of solar contribution, which reverses the expected inverse relationship between M13 BT and droplet size. After applying the M13 BT correction, the nighttime means become 16.0 for COT and 16.8 μm for CER—both within physically reasonable ranges and closely aligned with the daytime distributions. The COT, in contrast, shows relatively minor changes after correction, as it primarily depends on visible-band reflectance.

To further contextualize our results, panel (d) also includes daytime and nighttime CER from Hu et al. (2021), derived from CALIOP observations. Their retrievals also show larger nighttime CER than daytime, but the absolute values are systematically smaller than ours because their product includes global land and ocean scenes—where continental clouds generally have smaller droplets—whereas our analysis is limited to oceanic liquid clouds. Despite this offset, the direction and magnitude of the diurnal increase closely match our corrected VIIRS-based retrievals, supporting the physical plausibility of enhanced nighttime droplet size. The corrected CER peak (~17 μm) further highlights the effectiveness of the M13 BT adjustment in restoring physically consistent behavior, and the slightly larger nighttime COT and CER align with previous observational and modeling studies. Dong et al. (2014), using ground-based radar and microwave radiometer measurements from the ARM Mobile Facility at the Azores, found that nighttime marine boundary-layer clouds generally have higher LWP, thicker cloud layers, and thus slightly higher COT and CER due to stronger longwave cooling and the absence of solar heating. Likewise, Zhang et al. (2019) applied a satellite-based ML model trained with CALIOP and MODIS features (including lidar ratio, depolarization, and cloud-top temperature) and reported that nighttime CER is typically 2–3 μm larger than daytime on an annual average. Compared with these studies, our corrected nighttime retrievals show a consistent and physically plausible enhancement in COT and CER, demonstrating that the UNL-VRTM-based correction effectively removes solar-residual biases while preserving true diurnal microphysical variability.

Additional comparisons with the independent Version 4 CALIPSO Imaging Infrared Radiometer (CAL-IIR) Level-2 cloud microphysical

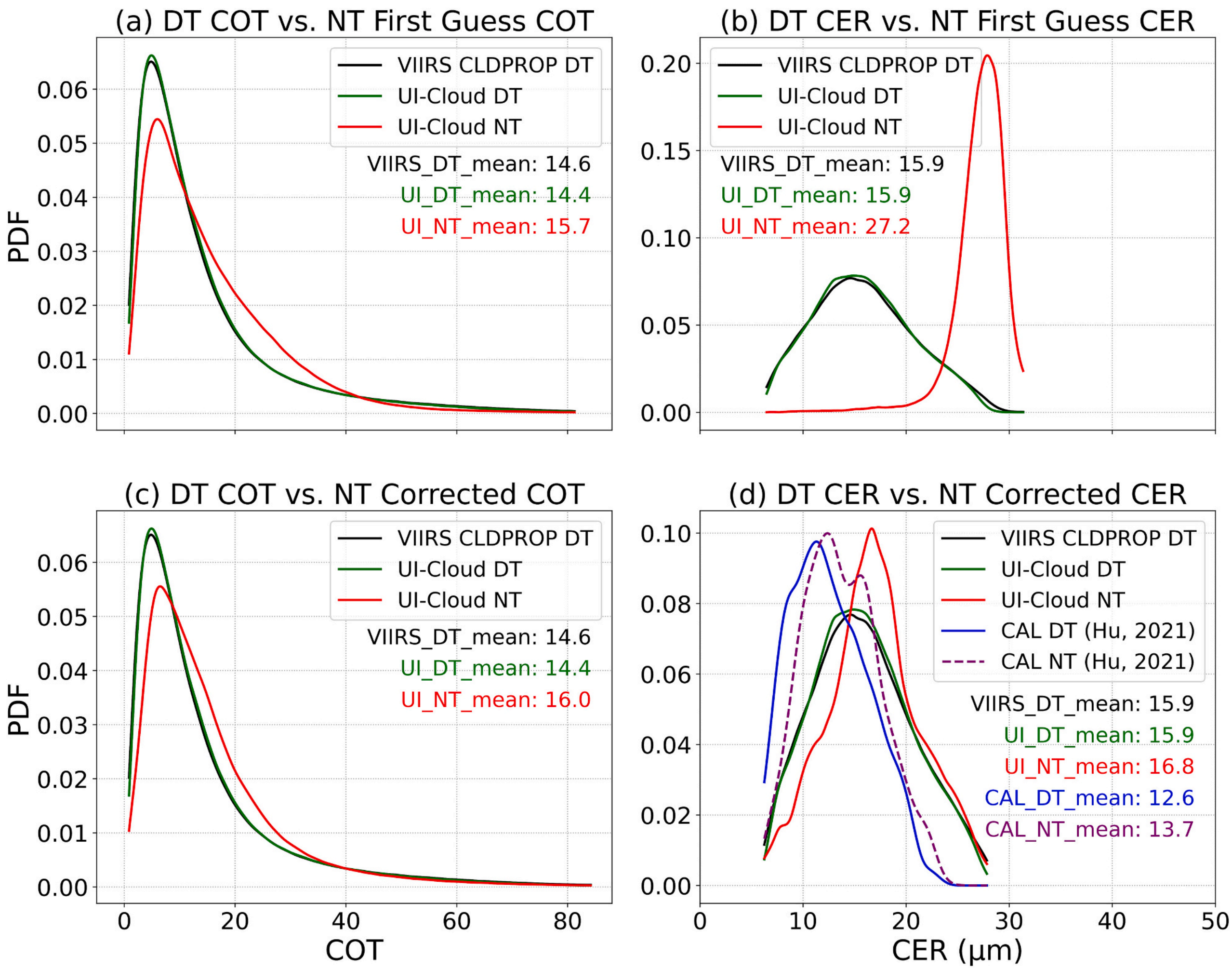

Fig. 9. Probability density functions (PDFs) of daytime VIIRS observations, ML retrievals, and nighttime ML retrievals for COT and CER on 2 September 2020. Panels (a–b) show the initial nighttime "first-guess" retrievals, while panels (c–d) present the results after applying the UNL-VRTM-based correction. Panel (d) also includes daytime and nighttime CER from the CALIOP-based product of Hu et al. (2021), which includes both land and ocean scenes, whereas our analysis is limited to oceanic clouds.

properties product are presented in the Supplementary Material (Figs. S6 and S7). CAL-IIR derives cloud particle size using the split-window thermal infrared technique (8.65, 10.6, and 12.05 μm) constrained by CALIOP scene classification (Garnier et al., 2021). For consistency with the present study, only high-quality oceanic liquid-cloud retrievals were retained using the recommended CAL-IIR quality-assurance criteria. Although the point-by-point agreement is weak, similarly weak agreement is also observed between CAL-IIR and the operational VIIRS CLDPROP CER product. This behavior is consistent with differences in retrieval physics and the relatively large uncertainty of the CAL-IIR liquid-cloud retrievals; Garnier et al. (2021) reported random uncertainties of approximately 45–50% for CAL-IIR liquid-cloud effective diameter retrievals. Therefore, perfect pixel-level agreement is not expected. Furthermore, CAL-IIR generally retrieves smaller CER values than the VIIRS-based retrievals, consistent with the findings of Garnier et al. (2021), who reported that CAL-IIR liquid-cloud particle sizes are systematically smaller than MODIS retrievals. Nevertheless, both datasets consistently exhibit larger nighttime CER than daytime CER in their probability density functions, providing additional independent support for the physical plausibility of the retrieved nighttime CER variability.

Fig. 10 compares the retrieved LWP with AMSR2 microwave observations to evaluate the physical consistency of the ML-derived cloud properties. The cal-LWP is the LWP calculated from the ML-retrieved COT and CER following Eq. (10). Panel (a) shows the baseline relationship between VIIRS CLDPROP LWP and AMSR2 LWP. Although the correlation is moderate (R ≈ 0.57), this agreement is consistent with previous global assessments between MODIS and AMSR-E (Seethala and Horváth, 2010). As discussed in Section 2.3, passive-microwave LWP retrievals exhibit substantial uncertainties, particularly for thin and inhomogeneous liquid clouds. Turner et al. (2007) reported that microwave LWP uncertainties are typically on the order of 20–35 g m^{-2} under ideal conditions but can increase to greater than 100 g m^{-2} for broken or inhomogeneous cloud scenes. Moreover, the same study reported inter-algorithm differences of up to ~40 g m^{-2}, corresponding to ~40–50% of the total LWP for thin clouds (LWP < 100 g m^{-2}). Thus, RMSE values on the order of 100–150 g m^{-2} are within the bounds of uncertainty of existing passive-microwave intercomparisons of LWP at global scale.

Panel (b) shows that the UI-Cloud ML daytime retrievals reproduce the LWP–AMSR2 relationship ($R = 0.56$, RMSE = 118.64 g m^{-2}) with nearly identical performance to VIIRS CLDPROP_L2 data products ($R = 0.57$, RMSE = 116.24 g m^{-2}), confirming that the model effectively captures the radiative–microphysical coupling learned from the training dataset. This consistency is further supported by the LWP probability density functions in panel (c), which exhibit similar distributional behavior between the ML-derived and VIIRS CLDPROP_L2 data products relative to AMSR2. Panels (d-f) display the nighttime ML retrievals

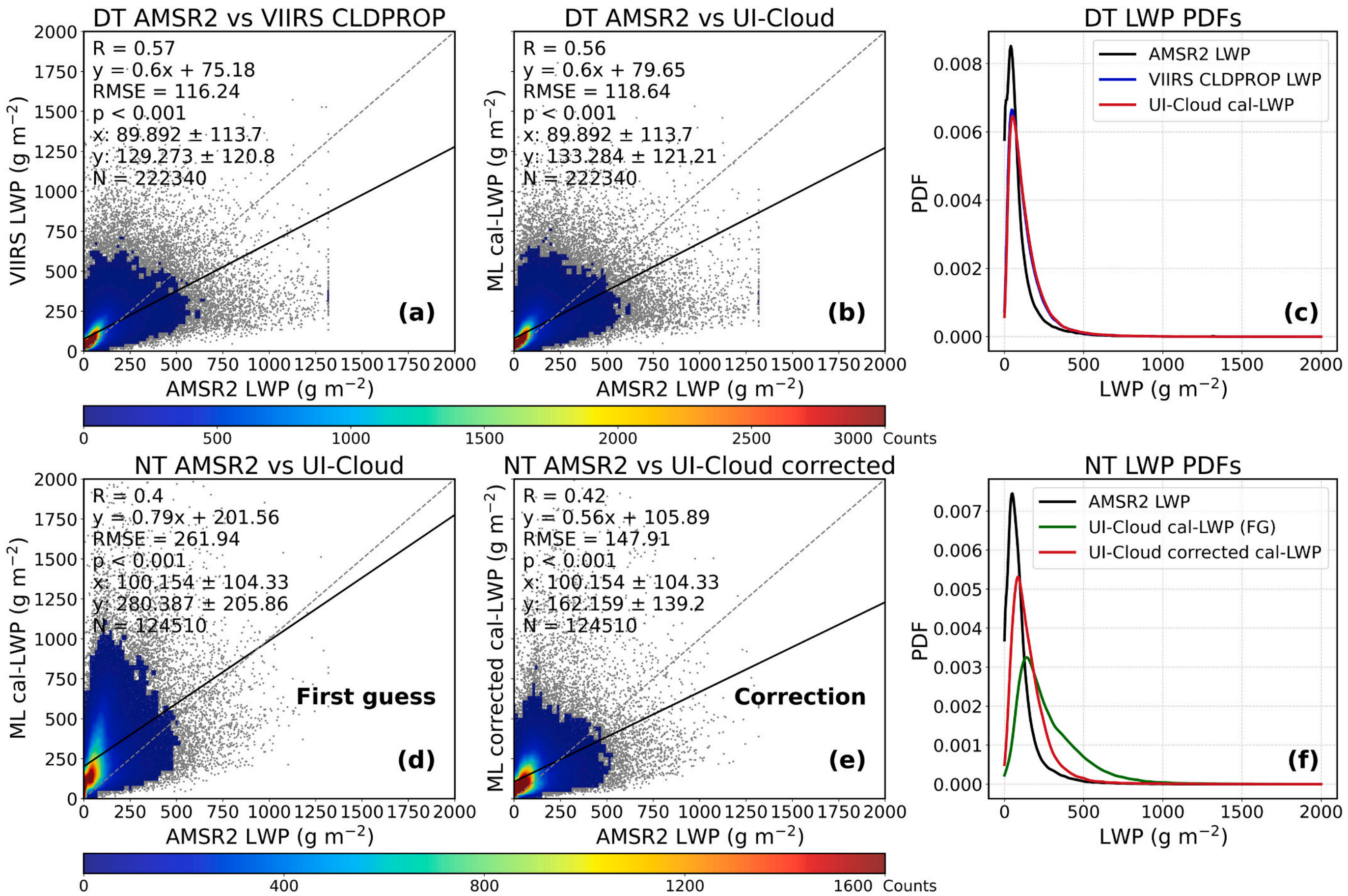

Fig. 10. Comparison of AMSR2 liquid water path (LWP) with VIIRS- and ML-derived LWP on 2 September 2020. (a, b) DT density scatter plots of AMSR2 versus VIIRS LWP and DT ML retrieval; (c) corresponding DT probability density functions (PDFs). (d, e) NT density scatter plots of AMSR2 versus NT ML initial retrieval (first guess, FG) and NT ML retrieval after correction; (f) corresponding NT PDFs.

before and after application of the UNL-VRTM-based correction. Following the M13 BT adjustment, the nighttime correlation improves

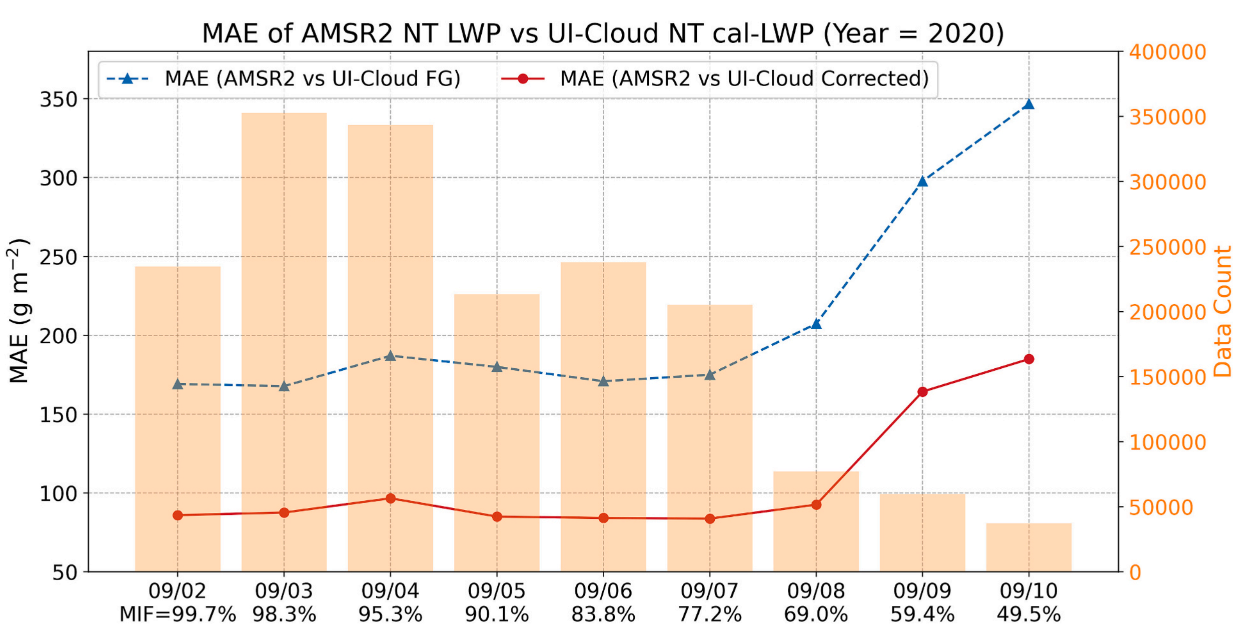

Fig. 11. Mean absolute error (MAE) of nighttime ML-derived LWP relative to AMSR2 observations from 2 to 10 September 2020, spanning moon illumination fractions (MIFs) from 99.7% to 49.5%. Blue dashed line: first-guess ML retrievals. Red solid line: UNL-VRTM-corrected results. Orange bars indicate the number of collocated VIIRS–AMSR2 grid cells used for comparison (after regridding both datasets to 0.1° resolution). (For interpretation of the references to colour in this figure legend, the reader is referred to the web version of this article.)

from $R = 0.4$ to 0.42, while RMSE decreases substantially from 261.94 to 147.91 g m^{-2}. The corresponding distributions also become more consistent with the daytime case, indicating that the correction not only reduces systematic bias but also restores the physical coherence of the retrieved liquid cloud field. Nighttime LWP errors remain larger than their daytime counterparts, which may be related to the lower signal-to-noise ratio of DNB observations and the lack of additional shortwave and near-infrared constraints available to nighttime retrievals. Further study is needed to verify this interpretation and to quantify the associated retrieval uncertainties. Overall, the corrected nighttime results align closely with the daytime benchmark, demonstrating that the ML + UNL-VRTM framework achieves diurnally consistent retrievals of cloud microphysical properties.

Nevertheless, direct pixel-level validation of nighttime COT and CER remains challenging because available reference products have different retrieval sensitivities, sampling characteristics, and uncertainties. Therefore, the assessment relies on multiple complementary lines of evidence, including spatial distributions, probability density functions, CALIOP- and CAL-IIR-based comparisons, and AMSR2-derived LWP evaluations. Accordingly, these comparisons should primarily be interpreted as evidence of the physical plausibility and reduced systematic biases of the nighttime retrievals rather than as direct validation of COT and CER retrieval accuracy.

To further evaluate the robustness of nighttime ML retrievals under varying lunar illumination, Fig. 11 presents the MAE of ML-calculated LWP, derived from COT and CER via Eq. 10, compared with AMSR2 observations for multiple nights between 2 and 10 September 2020, covering moon illumination fractions (MIFs) from 99.7% (full moon) to 49.5% (half-moon). Both VIIRS and AMSR2 datasets were regridded onto a common $0.1^\circ \times 0.1^\circ$ latitude–longitude grid to ensure consistent spatial comparison, with orange bars indicating the number of collocated grid cells used in the analysis. The results show that the corrected nighttime ML retrievals maintain high accuracy under bright-moon conditions (MIF $>$ 70%), achieving MAE values between 80 and 100 g m^{-2}, which is within the expected uncertainty of microwave LWP retrievals for thin marine clouds (Turner et al., 2007). As lunar illumination decreases below 60%, MAE increases markedly, reflecting weaker DNB signals and reduced lunar radiometric constraints. Nonetheless, the UNL-VRTM-corrected retrievals (red curve) consistently outperform the uncorrected first-guess results (blue dashed curve), demonstrating improved stability and physical consistency across a range of illumination levels. After 10 September 2020 (MIF $\approx$ 50%), valid nighttime DNB observations were no longer available, limiting further evaluation since DNB reflectance serves as a required input to the ML retrieval framework. These results indicate that the ML + UNL-VRTM framework remains reliable down to MIF $\approx$ 50%, establishing this as the practical lower limit for robust lunar-based nighttime retrievals.

Considering the lunar cycle, this translates to approximately 13–14 nights per month when the ML model can produce valid and physically consistent global nighttime cloud property retrievals, effectively bridging the diurnal gap in COT and CER observations.

5. Conclusions

This study developed and demonstrated a UI-Cloud, a ML framework for retrieving nighttime oceanic liquid-cloud optical and microphysical properties, COT and CER, from VIIRS observations using physically guided corrections and lunar illumination constraints. The approach leverages a daytime-trained neural network model, which jointly predicts COT, CER, and DNB TOA reflectance using multi-spectral thermal emissive bands (M13–M16), DNB, and geometric parameters as predictors. The model achieves high daytime performance (R $\approx$ 0.98) against VIIRS CLDPROP L2 retrievals, demonstrating strong generalization and radiometric consistency across global conditions.

To extend the retrieval capability into nighttime, an UNL-VRTM-based LUTs system was developed to quantify the physical offset between daytime and nighttime M13 BTs. This correction accounts for solar-residual contamination in the daytime thermal emissive bands and provides a consistent thermal baseline for nighttime applications. A dynamic scaling method based on RMSE thresholds was applied to constrain the correction according to model–observation agreement. The corrected nighttime M13 BTs align closely with daytime distributions, substantially improving the physical reliability of the nighttime retrieval inputs.

Nighttime retrievals conducted for the full-moon period (2 September 2020) demonstrate that the ML framework reproduces the global distribution of cloud properties with accuracy comparable to daytime retrievals. Before correction, the first-guess nighttime CER values were unrealistically high ($>$30 μm) due to the lower nighttime M13 BTs, but after correction, the CER and COT distributions aligned with climatological expectations and daytime references. For this day, the global mean nighttime COT and CER are 16.0 and 16.8 μm, respectively, slightly larger than the daytime means of 14.6 and 15.9 μm. This nighttime enhancement is consistent with prior studies showing that marine boundary-layer clouds often thicken and develop larger droplets at night due to strong longwave cooling. Validation against AMSR2 LWP confirms that the corrected nighttime retrievals are physically consistent, achieving correlation and RMSE performance close to the reference level between VIIRS and AMSR2 observations.

Further evaluation under varying lunar illumination fractions from full-moon to half-moon indicates that the ML + UNL-VRTM framework remains robust down to MIF $\approx$ 60%. Below this threshold, lunar radiance becomes too weak for reliable DNB-based retrievals. This corresponds to approximately 13–14 valid nighttime observation days per lunar cycle, ensuring regular global sampling to bridge the diurnal gap in cloud optical and microphysical datasets.

Overall, this work establishes a physically informed, data-driven pathway for retrieving nighttime oceanic liquid-cloud optical and microphysical properties from VIIRS. The integration of ML with the UNL-VRTM correction framework provides a robust approach for harmonizing daytime and nighttime cloud observations, offering new opportunities to study the full diurnal evolution of cloud processes and their radiative impacts.

The current framework is specifically designed for oceanic liquid-cloud retrievals, where surface radiative conditions are comparatively homogeneous and retrieval uncertainties are reduced. Extension to land surfaces and ice or mixed-phase clouds will require additional investigation and represent an important direction for future work. While the current model is trained using nine days of daytime observations and the nighttime evaluation primarily covers one lunar cycle, seasonal and broader environmental generalization have not yet been demonstrated. Nevertheless, the proposed retrieval framework is not restricted to a particular season and can be readily extended through the development of representative training datasets from different seasons or months, enabling broader applicability across a wider range of cloud and environmental conditions.

CRediT authorship contribution statement

Ying-Chieh Chen: Visualization, Validation, Methodology, Formal analysis, Data curation, Conceptualization. **Meng Zhou:** Supervision, Software, Methodology, Conceptualization. **Jun Wang:** Supervision, Methodology, Funding acquisition, Conceptualization. **Xi Chen:** Supervision, Methodology, Conceptualization. **Jing Zeng:** Resources, Investigation. **Yongxiang Hu:** Validation, Resources.

Declaration of competing interest

The authors declare that they have no known competing financial interests or personal relationships that could have appeared to influence the work reported in this paper.

Acknowledgements

This work was supported in part by NASA's Terra, Aqua, and SNPP Program under Award 80NNSC21L1976; in part by NASA's Modeling and Analysis Program (MAP) under Award 80NSSC21K1494; and in part by the NASA TEMPO–GOES/R Program under Award 80NSSC25K0221. The authors gratefully acknowledge the NASA LAADS DAAC and the NASA GMAO for providing the VIIRS and MERRA-2 datasets used in this study. The authors also thank Kerry G. Meyer (NASA Goddard Space Flight Center) for helpful guidance and documentation regarding the VIIRS cloud products. The authors also sincerely thank NASA's Distributed Active Archive Centers (DAACs) for providing the support to access the data used in this study. -

Appendix A. Supplementary data

Supplementary data to this article can be found online at https://doi.org/10.1016/j.rse.2026.115684.

Data availability

The satellite data from the VIIRS used in this study were obtained from the NASA LAADS DAAC (https://ladsweb.modaps.eosdis.nasa.gov/search/). The MERRA-2 reanalysis data were accessed from the NASA Global Modeling and Assimilation Office (GMAO) (https://gmao.gsfc.nasa.gov/reanalysis/MERRA-2/). CALIOP-based cloud microphysical retrievals from Hu et al. (2021) used in this study were kindly provided by the authors and are available upon reasonable request from the corresponding author, Yongxiang Hu (yongxiang.hu-1@nasa.gov).

References

Albrecht, B.A., 1989. Aerosols, cloud microphysics, and fractional cloudiness. Science 245, 1227–1230.
Chen, H., Xiong, X., Sun, C., Chen, X., Chiang, K., 2017. Suomi-NPP VIIRS day–night band on-orbit calibration and performance. J. Appl. Remote. Sens. 11, 036019.
Chen, Y.-C., Xue, L., Lebo, Z., Wang, H., Rasmussen, R., Seinfeld, J., 2011. A comprehensive numerical study of aerosol-cloud-precipitation interactions in marine stratocumulus. Atmos. Chem. Phys. 11, 9749–9769.
Dong, X., Xi, B., Wu, P., 2014. Investigation of the diurnal variation of marine boundary layer cloud microphysical properties at the Azores. J. Climate 27, 8827–8835.
Fan, J., Wang, Y., Rosenfeld, D., Liu, X., 2016. Review of aerosol–cloud interactions: mechanisms, significance, and challenges. J. Atmos. Sci. 73, 4221–4252.
Garnier, A., Pelon, J., Pascal, N., Vaughan, M.A., Dubuisson, P., Yang, P., Mitchell, D.L., 2021. Version 4 CALIPSO imaging infrared radiometer ice and liquid water cloud microphysical properties – part II: results over oceans. Atmos. Meas. Tech. 14, 3277–3299.
Gelaro, R., et al., 2017. The modern-era retrospective analysis for research and applications, version 2 (MERRA-2). J. Clim. 30, 5419–5454.
Hu, Y., et al., 2021. Liquid phase cloud microphysical property estimates from CALIPSO measurements. Front. Remote Sens. 2, 724615.
Iwabuchi, H., Yamada, S., Katagiri, S., Yang, P., Okamoto, H., 2014. Radiative and microphysical properties of cirrus cloud inferred from infrared measurements made by the moderate resolution imaging spectroradiometer (MODIS). Part I: retrieval method. J. Appl. Meteorol. Climatol. 53, 1297–1316.
Kawamoto, K., Nakajima, T., Nakajima, T.Y., 2001. A global determination of cloud microphysics with AVHRR remote sensing. J. Climate 14, 2054–2068.
Kieffer, H.H., Stone, T.C., 2005. The spectral irradiance of the moon. Astron. J. 129, 2887.
Kokhanovsky, A., 2019. Springer Series in Light Scattering: Volume 4: Light Scattering and Radiative Transfer. Springer.
Kummerow, C., Ferraro, R., Duncan, D., 2021. AMSR-E/AMSR2 Unified L2B Global Swath Ocean Products, Version 1. NASA National Snow and Ice Data Center Distributed Active Archive Center (DAAC). Data Set, 9YQRFKKEPUP4.
Lee, T.E., et al., 2006. The NPOESS VIIRS day/night visible sensor. Bull. Am. Meteorol. Soc. 87, 191–200.
Levy, R.C., et al., 2003. Evaluation of the moderate-resolution imaging spectroradiometer (MODIS) retrievals of dust aerosol over the ocean during PRIDE. J. Geophys. Res. Atmos. 108.
Lundberg, S.M., Lee, S.-I., 2017. A unified approach to interpreting model predictions. Adv. Neural Inf. Proces. Syst. 30.
Miller, S.D., et al., 2013. Illuminating the capabilities of the Suomi National Polar-orbiting Partnership (NPP) Visible Infrared Imaging Radiometer Suite (VIIRS) Day/Night Band. Remote Sens. 5, 6717–6766.
Miller, S.D., Turner, R.E., 2009. A dynamic lunar spectral irradiance data set for NPOESS/VIIRS day/night band nighttime environmental applications. IEEE Trans. Geosci. Remote Sens. 47, 2316–2329.
Minnis, P., Hong, G., Sun-Mack, S., Smith Jr., W.L., Chen, Y., Miller, S.D., 2016. Estimating nocturnal opaque ice cloud optical depth from MODIS multispectral infrared radiances using a neural network method. J. Geophys. Res. Atmos. 121, 4907–4932.
Nakajima, T., King, M.D., 1990. Determination of the optical thickness and effective particle radius of clouds from reflected solar radiation measurements. Part I: theory. J. Atmos. Sci. 47, 1878–1893.
Noh, Y.-J., et al., 2017. Cloud-base height estimation from VIIRS. Part II: a statistical algorithm based on A-train satellite data. J. Atmos. Ocean. Technol. 34, 585–598.
Platnick, S., et al., 2016. The MODIS cloud optical and microphysical products: collection 6 updates and examples from Terra and Aqua. IEEE Trans. Geosci. Remote Sens. 55, 502–525.
Platnick, S., et al., 2019. EOS MODIS and SNPP VIIRS Cloud Properties: User Guide for the Climate Data Record Continuity Level-2 Cloud Top and Optical Properties Product (CLDPROP).
Platnick, S., et al., 2020. The NASA MODIS-VIIRS continuity cloud optical properties products. Remote Sens. 13, 2.
Ramanathan, V., 1987. The role of earth radiation budget studies in climate and general circulation research. J. Geophys. Res. Atmos. 92, 4075–4095.
Ramanathan, V., Cess, R., Harrison, E., Minnis, P., Barkstrom, B., Ahmad, E., Hartmann, D., 1989. Cloud-radiative forcing and climate: results from the earth radiation budget experiment. Science 243, 57–63.
Román, R., et al., 2020. Correction of a lunar irradiance model for aerosol optical depth retrieval and comparison with star photometer. Atmos. Meas. Tech. Discuss. 2020, 1–29.
Rosenfeld, D., 1999. TRMM observed first direct evidence of smoke from forest fires inhibiting rainfall. Geophys. Res. Lett. 26, 3105–3108.
Seethala, C., Horváth, Á., 2010. Global assessment of AMSR-E and MODIS cloud liquid water path retrievals in warm oceanic clouds. J. Geophys. Res. Atmos. 115.
Spurr, R., Christi, M., 2019. The LIDORT and VLIDORT linearized scalar and vector discrete ordinate radiative transfer models: updates in the last 10 years. In: Springer Series in Light Scattering: Volume 3: Radiative Transfer and Light Scattering, pp. 1–62.
Spurr, R., Wang, J., Zeng, J., Mishchenko, M., 2012. Linearized T-matrix and Mie scattering computations. Journal of Quantitative Spectroscopy and Radiative Transfer 113, 425–439.
Stephens, G.L., 1978. Radiation profiles in extended water clouds. II: parameterization schemes. Journal of Atmospheric Sciences 35, 2123–2132.
Tao, W.K., Chen, J.P., Li, Z., Wang, C., Zhang, C., 2012. Impact of aerosols on convective clouds and precipitation. Rev. Geophys. 50.
Turner, D.D., et al., 2007. Thin liquid water clouds: their importance and our challenge. Bull. Am. Meteorol. Soc. 88, 177–190.
Twomey, S., 1977. The influence of pollution on the shortwave albedo of clouds. J. Atmos. Sci. 34, 1149–1152.
Walther, A., Heidinger, A.K., Miller, S., 2013. The expected performance of cloud optical and microphysical properties derived from Suomi NPP VIIRS day/night band lunar reflectance. J. Geophys. Res. Atmos. 118, 13230–13240.
Wang, C., Platnick, S., Meyer, K., Zhang, Z., Zhou, Y., 2020. A machine-learning-based cloud detection and thermodynamic-phase classification algorithm using passive spectral observations. Atmos. Meas. Tech. 13, 2257–2277.
Wang, C., Platnick, S., Zhang, Z., Meyer, K., Wind, G., Yang, P., 2016b. Retrieval of ice cloud properties using an optimal estimation algorithm and MODIS infrared observations: 2. Retrieval evaluation. J. Geophys. Res. Atmos. 121, 5827–5845.
Wang, C., Platnick, S., Zhang, Z., Meyer, K., Yang, P., 2016a. Retrieval of ice cloud properties using an optimal estimation algorithm and MODIS infrared observations: 1. Forward model, error analysis, and information content. J. Geophys. Res. Atmos. 121, 5809–5826.
Wang, J., et al., 2014. A numerical testbed for remote sensing of aerosols, and its demonstration for evaluating retrieval synergy from a geostationary satellite constellation of GEO-CAPE and GOES-R. J. Quant. Spectrosc. Radiat. Transfer 146, 510–528.
Wang, J., Van den Heever, S.C., Reid, J.S., 2009. A conceptual model for the link between Central American biomass burning aerosols and severe weather over the south Central United States. Environ. Res. Lett. 4, 015003.
Wang, Q., Zhou, C., Zhuge, X., Liu, C., Weng, F., Wang, M., 2022a. Retrieval of cloud properties from thermal infrared radiometry using convolutional neural network. Remote Sens. Environ. 278, 113079.
Wang, X., Iwabuchi, H., Yamashita, T., 2022b. Cloud identification and property retrieval from Himawari-8 infrared measurements via a deep neural network. Remote Sens. Environ. 275, 113026.
Xu, X., et al., 2019. Detecting layer height of smoke aerosols over vegetated land and water surfaces via oxygen absorption bands: hourly results from EPIC/DSCOVR in deep space. Atmos. Meas. Tech. 12, 3269–3288.
Yang, Y., et al., 2022. Machine learning-based retrieval of day and night cloud macrophysical parameters over East Asia using Himawari-8 data. Remote Sens. Environ. 273, 112971.
Zhang, F., Shao, X., Cao, C., Chen, Y., Wang, W., Liu, T.-C., Jing, X., 2024. Evaluation of VIIRS thermal emissive bands long-term calibration stability and inter-sensor consistency using radiative transfer modeling. Remote Sens. 16, 1271.

Zhang, Y., et al., 2019. Retrieving the microphysical properties of opaque liquid water clouds from CALIOP measurements. Opt. Express 27, 34126–34140.
Zhao, Z., Zhang, F., Wu, Q., Li, Z., Tong, X., Li, J., Han, W., 2023. Cloud identification and properties retrieval of the Fengyun-4A satellite using a ResUnet model. IEEE Trans. Geosci. Remote Sens. 61, 1–18.
Zhou, M., et al., 2021. Nighttime smoke aerosol optical depth over US rural areas: first retrieval from VIIRS moonlight observations. Remote Sens. Environ. 267, 112717.